UNIVERSITY OF UTRECHT

DEBUY INSTITUTE OF NANOMATERIALS SCIENCE
DEPARTMENT OF PHYSICS

COLD ATOM NANOPHOTONICS GROUP

Using an Optical Conveyor for Light-Matter Interaction Experiments

---

Konstantinos Voutyras

2017

Supervisors:
Dr. Dries van Oosten
A.J. van Lange, MSc

Dedicated to Rob and Eva

Abstract

In this work, we cool Rubidium atoms to the Doppler limit. After atoms were cooled, we use two purely optical traps, an Optical Dipole Trap (ODT) and a standing wave trap (optical conveyor) to transport them. We have optimized the performance of the standing wave trap and succeeded to slowly transport 10^5 traps and cools atoms to the surface of a nanophotonic sample located 5 mm from the loading point. We calibrated the required optical power during absorption imaging for the accurate and reproducible calculation of the number of trapped atoms. A 200 nm thin free-standing Silicon-Nitride slab waveguide was used to probe interactions between atoms and resonant light in the guided mode. The propagating mode has an evanescent tail that extends further than the physical dimensions of the waveguide. Bringing atoms to the resonant field can trigger interactions between light and atoms. We succeeded in coupling light in and out of the waveguide and built a dedicated imaging section for the transmission. Last, we performed a reference experiment to determine the response of the optical setup, without the presence of atoms at the proximity of the slab waveguide.

Contents

Chapter 1

Introduction

The first observation of a Bose-Einstein Condensation (BEC) in 1995 [1] allowed the study of quantum phenomena at a macroscopic scale. The study of atoms cooled to a temperature of a few micro Kelvin above absolute zero, enables research of quantum systems while having extensive control over the macroscopic properties of an ensemble of atoms.

The field of Nanophotonics, studies optical phenomena and techniques at the nanometer scale; that is near or beyond the diffraction limit of light [6]. Nanostructures with a high refractive index contrast can confine light and give rise to high peak-intensities, steep near-fields etc. Bringing quantum systems close to the near-field of guided light can probe fascinating interactions.

At the beginning of the project the experimental work focused on relating the intensity during absorption imaging to the calculated number of atoms. From these experiments we determined the optimal. Next, we optimized the transport of cold Rubidium atoms (^{87}Rb) using the standing-wave trap and we studied the properties of that motion (lattice velocity, atom cloud dimensions, atom rates). We succeeded in observing light transmitted through the nanophotonic waveguide.

Last, we extended the imaging section of the setup by adding an extra detector. The new scheme allowed us to capture the light coupled out of the waveguide with simultaneous operation of one or more detectors.

The structure of this thesis is as follows. The second chapter outlines the theory for trapping and cooling Rubidium atoms to

the Doppler limit using all-optical trapping and Magneto-Optical Trapping (MOT). At the end of the chapter we discuss the properties of the optical modes propagating in the waveguide.

The third chapter outlines the operation of our experimental setup. The technical details are explained starting from different parts of the vacuum system, to the magnetic fields, and the MOT lasers and how these make up two-stage MOT configuration. The chapter continues with the description of the two all-optical traps, the ODT and the Optical Conveyor. Atoms are transported to the surface of nanophotonic samples by means of a steering mechanism in the horizontal plane (ODT) and an elevation mechanism with which the optical conveyor is equipped.

We describe the principle of absorption imaging and how this is used for calculating the number of atoms inside the cloud. In the last section, we describe the implementation of the imaging section for the atoms and the transmission imaging.

The final chapter contains the experimental approach and results obtained from improving the operation of the optical conveyor. We performed an experiment where we linked the intensity of the imaging beam to the number of atoms calculated during absorption imaging. Following, we performed a series of experiments with which we selected the optimal parameters for the conveyor motion. We discovered and eliminated two powerful static lattices, which improved the atom transfer efficiency by approximately 30%. We conducted a series of experiments where we displaced the conveyor and driven atoms towards the surface of a sample. We calculated the rate with which atoms are lost due to the collision and used this number to estimate the length of the atom cloud.

Finally, we succeeded in coupling light into a nanophotonic slab waveguide and performing a reference experiment to determine the the baseline response of the system.

Chapter 2

Ultracold Atoms

This chapter introduces the theoretical framework of atom cooling and trapping. Within the classical approach, the atom is treated as a dipole. We present a detailed derivation of the scattering rate and the trapping potential. Extending this discussion to 2-level systems, we take into account the saturation of the scattered optical power within optical fields. We introduce the principles of Doppler cooling using purely optical cooling, the Zeeman splitting and finally Magneto-Optical Trapping and cooling. The mode profile and effective index of light propagating inside a nanophotonic waveguide for TE, TM polarizations is given. From those properties, we select the desired polarization for our experiments. The chapter is concluded with the requirements for the experimental detection of interactions between light and matter.

2.1 Atoms as dipoles

In this section we treat atoms as Lorentz oscillators interacting with the electric field of a laser beam. In our analysis we will treat the electric field as a classical time-harmonic field of the form

$$\vec{E}(t) = \vec{E}_0 e^{i(\omega t - \vec{k}\cdot\vec{r})} + c.c. \tag{2.1}$$

We consider that the atomic dipole consists of a nucleus and an outer electron. Placing the atom inside an optical field causes the atom to exhibit a dipole moment. The forces that act on the electron are a spring-like restoring force and a viscous, damping force with a rate Γ that denotes the power dissipated from the field. In this

model, the equation of the electron motion obtains the form of a driven oscillator with the damping force proportional to its velocity. The differential equation of the driven electron will be

$$m_e\ddot{x}(t) + m_e\Gamma\dot{x}(t) + m_e\omega_0^2 x(t) = -eE(t). \tag{2.2}$$

The solution of 2.2 has two terms. The first term is the solution of the damped oscillation (transient)

$$x_{\mathrm{D}} = e^{\Gamma t}(Ae^{i\omega' t} + Be^{-i\omega' t}), \tag{2.3}$$

where A, B are constants which depend on the initial conditions.

When the Lorentz oscillator is placed inside an oscillating field, it will oscillate with the frequency of the field. The steady-state solution will be

$$x_{\mathrm{S}} = Ce^{-i\omega t}. \tag{2.4}$$

If we replace 2.4 in 2.2 we will end up with the oscillation amplitude

$$C = \frac{E_0}{i\omega\Gamma + m_e(\omega_0^2 - \omega^2)}. \tag{2.5}$$

The total solution is given by the superposition of the 2.3 and 2.4. When an atom is placed into the beam, it will exhibit a dipole moment

$$\vec{p} = q\vec{x}. \tag{2.6}$$

There is a linear relation between the dipole moment and the electric field as

$$\vec{p} = \alpha(\omega)\vec{E}, \tag{2.7}$$

where α is the polarizability.

$$\alpha(\omega) = \frac{e^2}{m_e}\frac{1}{\omega_0^2 - \omega^2 - i\omega\Gamma} = \frac{e^2}{m_e}\left(\frac{\omega_0^2 - \omega^2}{\left(\omega_0^2 - \omega^2\right)^2 + \left(\omega\Gamma\right)^2} + \frac{i\omega\Gamma}{\left(\omega_0^2 - \omega^2\right)^2 + \left(\omega\Gamma\right)^2}\right), \tag{2.8}$$

where the damping rate Γ equals to

$$\Gamma = \frac{e^2}{m_e}\frac{\omega^2}{6\pi\epsilon_0 c^3}. \tag{2.9}$$

The real part of the polarizability describes the potential energy of the dipole inside the electric field. The imaginary part on the other hand, $\alpha(\omega)$ describes the power absorbed by the dipole under the influence of the field. In other words, $\mathrm{Re}(\alpha)$ describes an interaction of conservative nature whereas $\mathrm{Im}(\alpha)$ involves energy dissipation. [13]

The real part of $\alpha(\omega)$ determines the dipole (trapping) potential as

$$U_{dip} = -\frac{1}{2\epsilon_0 c} Re(\alpha) I(r), \tag{2.10}$$

where $I(r) = \frac{\epsilon_0 c}{2}|E|^2$ is the field intensity

$$= -\frac{3\pi c^2}{2\omega_0^3}\left(\frac{\Gamma}{\omega_0 - \omega} + \frac{\Gamma}{\omega_0 + \omega}\right) I(r). \tag{2.11}$$

The power dissipated by the oscillator is related to the imaginary part of polarizability as

$$P_{abs} = -\frac{\omega}{2\epsilon_0 c} Im(\alpha) I(r) \tag{2.12}$$

The absorbed power is re-emitted in the form of dipole radiation. The emission is described by the scattering rate

$$\Gamma_{sc}(r) = \frac{P_{abs}}{\hbar\omega} = -\frac{3\pi c^2}{2\hbar\omega_0^3}\left(\frac{\omega}{\omega_0}\right)^3\left(\frac{\Gamma}{\omega_0 - \omega} + \frac{\Gamma}{\omega_0 + \omega}\right)^2 I(r). \tag{2.13}$$

If we rewrite 2.13 in terms of the saturation intensity

$$I_{\mathrm{sat}} = \frac{\hbar\omega_0^3\Gamma}{4\pi c^2} \tag{2.14}$$

that would be

$$\Gamma_{sc}(r) = -\frac{6}{\Gamma}\left(\frac{\omega}{\omega_0}\right)^3\left(\frac{\Gamma}{\omega_0 - \omega} + \frac{\Gamma}{\omega_0 + \omega}\right)^2 \frac{I(r)}{I_{\mathrm{sat}}}. \tag{2.15}$$

It can be seen from Figure 2.1, that the real part of the polarizability goes to zero as ω approaches ω_0. At ω_0 the imaginary part

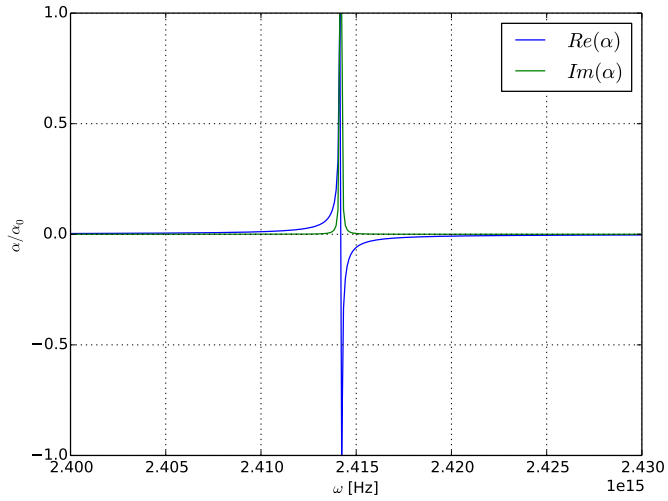

Figure 2.1: Polarizability as calculated from the Lorentz model.

obtains its maximum value. At resonance, the trapping potential becomes zero and the power dissipation becomes maximum.

In order atom trapping to be realized, the scattering rate should remain low. We introduce the detuning δ of the radiation frequency with respect to the transition frequency as $\delta = \omega - \omega_0$. In the case of a small detuning $\omega_0 - \omega \approx \omega_0$, $\frac{\omega}{\omega_0} \approx 1$, we can apply the Rotating Wave Approximation and omit the quickly rotating term $\omega + \omega_0$. The classical equations are simplified to

$$U_{dip} = \frac{3\pi c^2}{2\omega_0^3} \frac{\Gamma}{\delta} I(r) \tag{2.16}$$

and

$$\Gamma_{sc} = \frac{3\pi c^2}{2\omega_0^3} \left(\frac{\Gamma}{\delta} \right)^2 I(r) \tag{2.17}$$

By dividing these equations we arrive at a relation between the scattering rate and the trap depth.

$$\hbar \Gamma_{sc} = \frac{\Gamma}{\delta} U_{dip}, \tag{2.18}$$

These equations have some interesting implications. First, the sign of the detuning determines the trapping potential shape. Atoms can be trapped at the minimum of the potential. When the detuning is negative (red detuning) the laser beam provides an attractive potential so atoms will be trapped at the intensity maxima.

The conclusion that can be drawn, already from the classical treatment, is that atoms cannot be trapped near their resonance due to the trapping potential being zero.

Forces acting on atoms

Already from equations 2.10 and 2.15 it can be deduced that two different forces act on atoms interacting with an optical field. The first force is the result of the dipole potential

$$F_{dip} = -\nabla U_{dip}. \tag{2.19}$$

The second force arises from the fact that power (photon) transferring rate implies a rate of momentum transfer, which is directly related to a force as

$$F_{rad} = \frac{d\vec{p}}{dt} = \hbar\vec{k}\Gamma_{sc}. \tag{2.20}$$

Transfer of momentum from the field to the atom results to a change in the total momentum, also known as recoil. In short, there are two main forces which govern the interactions of light and matter

1. **The dipole force**: It is the result of coupling the atomic dipole moment with the electric field. Due to its conservative nature, it is used for trapping atoms. As dipole forces are independent of the saturation, they can be made infinitely strong.

2. **The scattering force**: It is a dissipative force associated with the difference in momentum when an atom emits light outside the laser beam. It involves energy exchange between the atom and the laser field. This is primarily important in cooling atoms. The force is also referred as radiation pressure or recoil force.[13]

Saturation

Extending the above results to two-level atoms with a ground state $|g\rangle$ and excited state $|e\rangle$, the scattering force exerted by an atom will be

$$\vec{F}_{rec} = \hbar\vec{k}R_{sc} = \hbar\vec{k}\Gamma\frac{s_0}{1+s_0+4\delta/\Gamma^2}, \tag{2.21}$$

where Γ is the natural linewidth of the $|g\rangle \rightarrow |e\rangle$ transition, s_0 is the saturation parameter which equals to I/I_{sat} and $\delta = \omega - \omega_{eg}$ is the frequency detuning with respect to the transition frequency.

For an ensemble consisting of N 2-level atoms,the maximum recoil force will be $N\hbar\vec{k}\Gamma/2$ when $s_0 \rightarrow \infty$ (I$\rightarrow \infty$) as no more than 50% of the population can be found in the excited state.

The required intensity for saturating the scattered power of ^{87}Rb is 1.66933 mW/cm^2. The significance of this quantity becomes apparent when the number of atoms in a specific volume needs to be calculated. Throughout this project, we have been very concerned with the the intensity used for probing the atoms. Knowing exactly the intensity experienced by the atoms enables the accurate and reproducible determination of their number.

2.2 Cooling and Trapping Atoms

In the "low saturation" regime, the contributions of the dipole and the scattering force are employed in cooling and trapping the atoms. The experimental parameters are tuned to provide larger scattering or dipole forces respectively. Each of these functions is promoted at different parts of the experimental setup used to enhance either cooling or trapping.

2.2.1 Doppler cooling

In a simple configuration, an atom with velocity $\vec{v}$ is placed inside two identical, counter-propagating beams. Owing to the Doppler effect, it will experience a frequency difference of $\Delta_{\pm} = \omega \pm \vec{k}\cdot\vec{v}$, in the laboratory frame as illustrated in Figure 2.3). For small

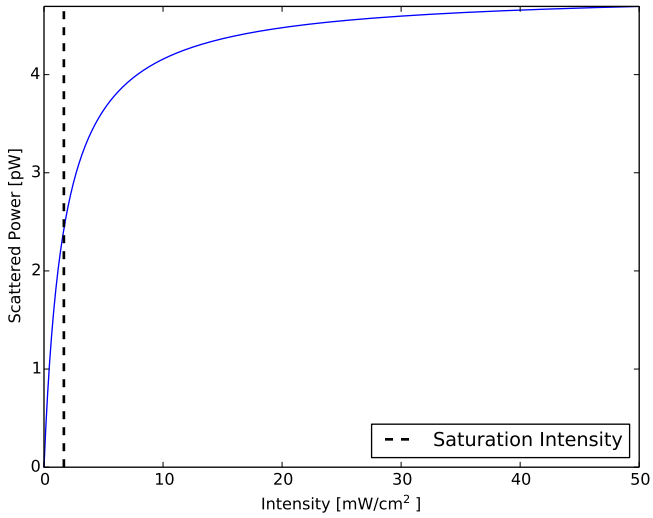

Figure 2.2: Power scattered from a 2-level system as a function of probe intensity.

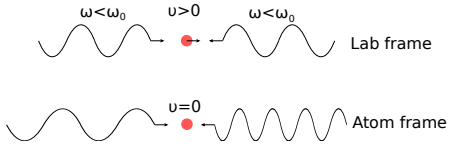

Figure 2.3: Doppler shift of the optical field experienced by the atom due to its thermal velocity.

velocities, the frequency difference will create a net force [13]

$$F = \frac{\hbar k^2 \Gamma^3}{2} \frac{\delta}{[\delta^2 + (\Gamma/2)^2]^2} \frac{I}{I_{\text{sat}}} \upsilon. \tag{2.22}$$

The force is attractive when $\delta < 0$ (red detuning). Its viscous damping nature can trap atoms with low velocity inside a region known as Optical Molasses.

When the Doppler shift matches the transition frequency ω_{eg}, the atom can absorb the light and get to the excited quantum state, while decreasing its velocity. Since thermal velocity is directly related to the atom temperature, a velocity decrease will result in cooling the atom. Photon re-emission will occur isotropically re-

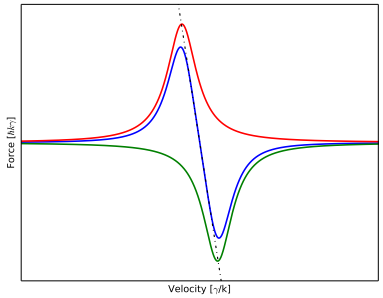

Figure 2.4: The force excerted on slowly moving atoms inside an optical molasses as a function of their velocity. The dotted lines depict the force from each beam, the solid line denotes their sum. The linear region for low velocities creates a restoring force. For high velocities, the force approaches zero. Adopted from [9].

sulting in a net recoil force. The temperature limit that can be reached with an one-dimensional configuration is $T_{\mathrm{D}}= 145\,\mu\mathrm{K}$. Due to the Doppler effect, atoms experience a scattering force, dependent on the velocity. The scattering force creates thus a friction force.

A potential trap can be then created only with motion-specific forces that exhibit a zero-point within the molasses. The zero-point field can be created by using magnetic fields with a zero-point. Such fields are generated by placing the coils in an Anti-Helmholtz configuration. In this configuration, the trapping efficiency can be significantly improved by employing relatively weak magnetic fields while using moderate optical powers.

2.2.2 Magneto-Optical Trapping

The atomic excited state has three degenerate hyperfine states. The application of an inhomogeneous magnetic field gives rise to the anomalous Zeeman effect.

In an one-dimensional MOT the magnetic field would exhibit a linear inhomogeneity

$$\nabla \vec{B} = 0, \tag{2.23}$$

which leads to

$$\vec{B} = \hat{z}\frac{d\vec{B}}{dz} \tag{2.24}$$

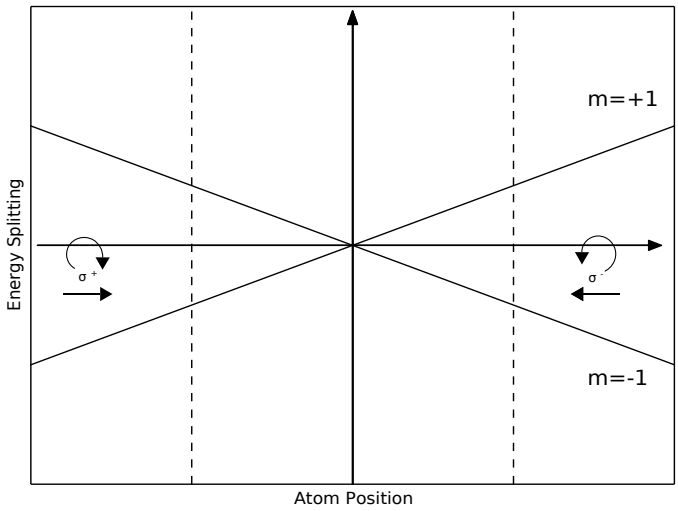

Figure 2.5: Zeeman energy splitting as a function of the atom distance from the center of the trap.

We assume the total angular momentum of the atomic ground state to be $J_g = 0$ and the angular momentum of the excited state $J_e = 1$ [7]. The application of the magnetic field causes the states to split by

$$\Delta E = g_j m_j \mu_B \Delta B, \tag{2.25}$$

where the Landé factor,g_j, is equal to

$$g_j = \frac{1 + (J(J+1) + S(S+1) - L(L+1)}{2J(J+1)}. \tag{2.26}$$

As it can be seen from eq. 2.25, the energy splitting is a function of distance from the center of the trap. Each hyperfine state m=(-1, 0, +1) can be probed using $(\sigma^-, \pi, \sigma^+)$ polarized light respectively. For an atom resting at z>0, the m=+1 state will shift up, while the m=-1 will shift down, closer to the energy of the cooling laser. Hence it will scatter more than the m=+1 state. Decay from each of these states, introduces an additional restoring recoil force towards $\vec{B} = 0$, which coincides with the center of the trap. The thermal velocity of the atom will induce a small correction to the energy shift equal to $\omega_D = \vec{k} \cdot \vec{v}$ added to the shift experienced by the optical field. If, for example, the atom moves towards the laser beam this will result to

a blue shift, enhancing the scattering of the m=-1 state.

2.3 Light inside a two-dimensional dielectric waveguide

Evanescent fields are of high importance in the emergent field of nanophotonics. Their formation occurs from confining light in structures of subwavelength dimensionality. This property serves as a useful tool in numerous applications including sensing, microscopy etc [6].

2.3.1 Nanophotonic Waveguide

The nanophotonic waveguide we used for our experiments consists of a SiN slab with thickness $\lambda/4$. The thickness allows only the existence of a TE_{00} and a TM_{00} mode. Either mode can be selected by changing the polarization of the incident beam. The optical confinement causes the mode to form an evanescent tail extending above (and below) the sample. Atoms brought to the sample surface can absorb photons of the evanescent tail if the radiation is resonant.

Intensity profile inside the waveguide

The intensity profile of the TE and TM mode propagating inside the slab is illustrated in 2.6. The gray area indicates the slab.

The intensity of the transverse electric mode drops below $1/e^2$ inside the slab. The transverse magnetic mode intensity, on the other hand, drops below $1/e^2$ at approximately 140 nanometers above the sample surface. This means that interactions between atoms and TM polarized light will be stronger, as the mode extends further into free space.

2.3.2 Atoms interacting with evanescent light

A variety of different experiments with evanescent fields interacting with matter using atomic mirrors, hollow fibers, prisms etc. have been demonstrated in literature [11]. A major challenge is to maintain coherence of the atomic wavefunctions. Already by using simple structures, such as wide dielectric atomic mirrors, we can realize a

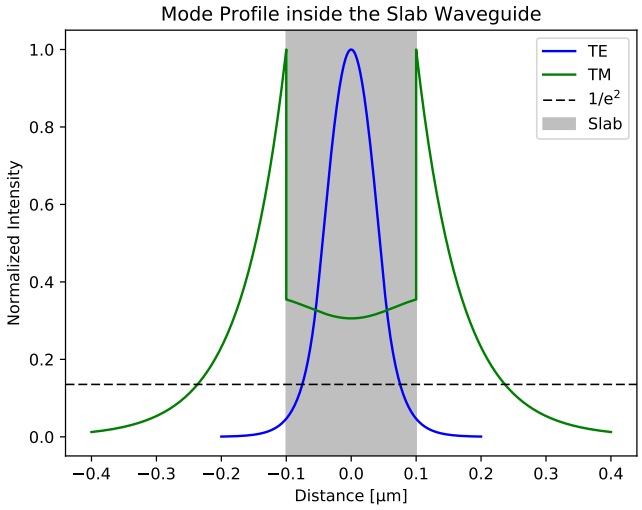

Figure 2.6: Normalized intensity profiles of the slab waveguide for both TE and TM modes.

few aspects useful for our experiments. The interaction strength depends on the intensity and the detuning. At a first stage, the light needs to be close to resonance. At a second stage we need to obtain a strong interaction, in order to be experimentally detected. Hence, we end up to the following requirements:

1. The intensity of the evanescent field needs to be below I_{sat}. Light scattered by atoms will be significant when the intensity is higher than 1/e of its value at the edge of the waveguide.

2. The atom velocities need to be well defined. Atoms with high thermal velocities will diffusively scatter over the barrier resulting in incoherence. On the other hand, atoms that graze over the surfaces with very low thermal velocity will experience small forces. This will allow them to reach the sample surface and attach on it by creating Van der Waals bonds.

3. The atom number needs to be high enough to ensure that adequate power can be scattered and the interaction can be experimentally detected.

Chapter 3

Experimental Setup

In this chapter, we introduce the building blocks that make up our experiment. A short description of the vacuum operation is followed by a technical description of the MOT magnetic fields and lasers. The chapter contains the latest configuration of the optical setup of Optical Dipole Trap. Special emphasis is placed on the optical conveyor regarding the loading and the improvements made in the atom transporting scheme. We describe the setup for the atom and transmission imaging followed by explaining the principle of absorption imaging performed at the locations of both the ODT and the optical conveyor. We present the optical setup for imaging the transmission and we describe how the signal acquisition takes place. Finally, we describe the optical properties of the samples used in these experiments.

3.1 Vacuum System

The experiment takes place inside a series of vacuum chambers. The setup consists of three parts, the 2D chamber, the main chamber (3D) and the load-lock chamber. The main chamber is evacuated to pressure in the order of 2 10^{-10} mbar. High vacuum minimizes elastic collisions between trapped atoms and air molecules. This provides longer atom lifetimes necessary for transporting and probing atoms.

The chamber of the two-dimensional MOT consists of a cylindrical PYREX tube where atoms get trapped in a cigar-shaped cloud. The 2D chamber communicates with the main chamber via a 1.1

mm hole. The pressure difference between the 2D and 3D chamber is approximately two orders of magnitude. The pressure gradient gives rise to differential pumping. Due to the low pressure, atoms are transferred via free molecular flow through the aperture. This allows to maintain a high pressure difference between the two chambers.

Natural Rb initially originated from an oven, has adsorbed and formed aggregates on the walls of the tube. Thus, the pumping rate corresponds to the desired pressure in the 2D chamber which is $5 \cdot 10^{-7}$ mbar (Rubidium vapour pressure). There is an adequate quantity of Rb inside the 2D chamber, so the oven is not operating during the experiments.

Finally, the load-lock chamber allows us to perform sample exchanges without breaking the vacuum of the main chamber. It is separated from the main chamber by means of a hermetically sealed valve which opens only for exchanging samples. The chamber is equipped with two manipulators: a fork and a base. The fork moves the samples into the main chamber and the base has three pockets for storing samples in the load-lock. The load-lock chamber is kept at pressure in the order of $3 \cdot 10^{-9}$ mbar. Upon venting it for sample exchange, the vacuum can be restored in a few days. A detailed schematic of the vacuum system can be found in Figure 3.1.

3.2 MOT Coils

As discussed in 2.2.2, the trapping efficiency can be significantly improved by employing inhomogeneous magnetic fields that causes splitting between the degenerate states. The inhomogeneous fields are created with anti-Helmholtz configuration. Inhomogeneous magnetic field is created with opposite currents running through two opposing cylindrical coils. The field "zero" coincides with the center between the coils and is located at the center of the chamber.

The coils of both stages operate in anti-Helmholtz configuration. Atoms located out of the center experience forces of viscous and restoring nature due to simultaneous operation of the magnetic fields and the cooling lasers.

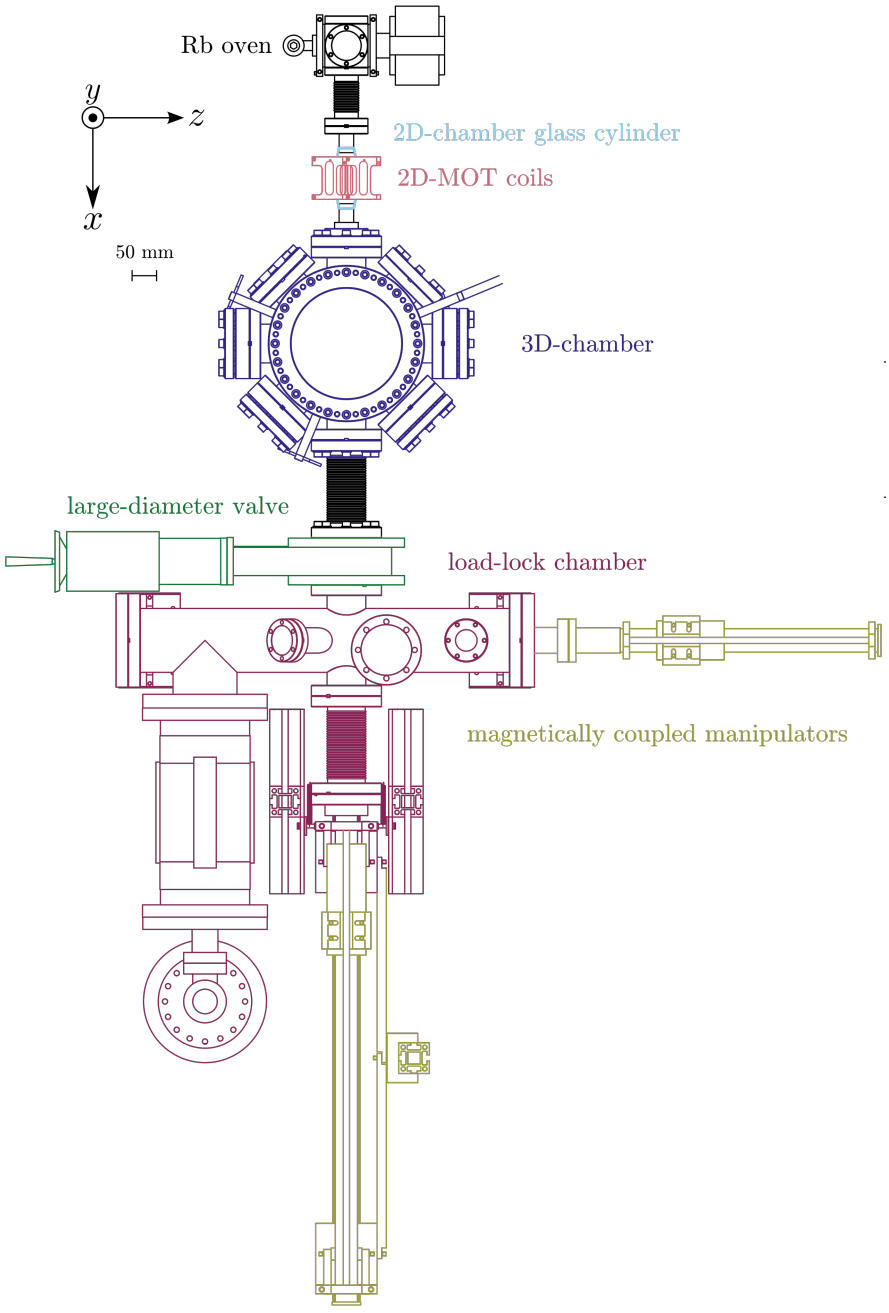

Figure 3.1: Schematic of the vacuum chamber.

2D Coils

The process is assisted by four water-cooled coils shaped as rounded rectangles and mounted around the axis of the 2D chamber. This shape produces enhanced overlap with the cigar-shaped atom cloud. Current of 1.98A with opposite directions runs continuously through opposing coils, producing a magnetic field gradient of 7.43 G/cm at the center of the trap. Power dissipation is achieved by the internally water-cooled holder.

3D Coils

The main chamber is surrounded by two water-cooled coils. The Zeeman splitting is zero at the center of the chamber, producing a restoring force towards the center of the chamber. The current switches on at the beginning of each cycle and gradually ramps down at the end of it. Current of 15.0 A produces a field gradient of 16.01 G/cm. The heat produced by the coils is dissipated by the water-cooling system.

Compensation coils

During each experimental cycle the 2D and 3D coils operate simultaneously. The small distance between the two MOTs causes the magnetic field of the 3D-MOT to interfere with that of the 2D-MOT. The interference causes a non-zero Zeeman splitting at the center of the 2D trap. The impact is minimized by adding a pair of coils at either sides of the 3D chamber. The first coil minimizes the magnetic field gradient into the 2D-MOT while the second counteracts the influence of the compensation coil to the position of the magnetic "zero" inside the 3D chamber. The compensation coils operate at 65 V, 2.5 A. These coils are not water-cooled and their steady-state temperature is around 66 ° C.

More information on the operation of the coils can be retrieved from [4], [5].

3.2.1 MOT lasers

Atom cooling and trapping is realized using five lasers. The configuration contains a reference laser and two sets of cooling and repumping lasers.

Reference Laser

The laser is used as reference frequency for the experiment, for locking the cooling lasers, probing the atoms as well as for the implementation of the "push" beam. Setting the laser frequency involves "locking" it to some reference. The locking frequency is obtained by Rb saturated Doppler spectroscopy. The laser is locked at the (1,3) transition crossover[1].

The reference beam is shifted to resonance using an AOM[2]. Resonant light is used for imaging at the center of the main chamber and above the sample surface. Part of the reference beam is split to a path with a separate AOM and it is used for coupling light into a nanophotonic sample. The imaging, push and probe light are coupled into separate fibers and trasported to the main table.

Cooling lasers

The high-power cooling lasers are offset-locked with respect to the reference light locked in the F=2 $\rightarrow$ F'=3 crossover frequency as seen in Appendix A.1. The 2D-MOT cooling light is red-detuned by 204.0 MHz, whereas the 3D-cooling light is red-detuned by 193.0 MHz. The small detuning is achieved by an external electronic system. The high powers are achieved by seeding the laser light into tapered amplifiers.

Repumping lasers

The low-powered repumping light is used to enhance the number of atoms in the cooling scheme. They are locked in the F=1 $\rightarrow$ F'=2 and they are used to excite atoms towards the two-level cooling cycle.

[1] Crossover frequencies are present for systems with more than two states in a counter-propagating beam configuration. If two transition frequencies with the same ground state occur within the same Doppler-broadened peak, atoms can experience both beams resonant for either of the transitions. A crossover peak will rise right between those two frequencies. The strength and position of the peak makes it ideal for laser locking.

[2] The AOM contains a crystal which is modulated with an electric field of acoustic frequency (radio frequency). The modulation produces a running wave which changes the refractive index of the material causing the incident beam to get diffracted. Different orders of refraction produce different beams with Doppler shifted frequencies. The beams exit the AOM at a slightly different angle than the incident beam allowing us to distinguish between the diffraction orders.

MOT laser powers

2D Cooling laser	92.0 mW
2D Repumping laser	4.2 mW
3D Cooling laser	84.5 mW
3D Repumping laser	1.2 mW

Table 3.1: MOT Laser powers used during the experiments.

The cooling and repumping light for each MOT is coupled into the same fiber and transported to the main table.[4]

The optimal powers of the cooling and repumping lasers for efficient operation are summarized in 3.1. The values are measured on the main optical table, in front of the outcoupler of each fiber.

3.3 Cooling and Trapping Atoms

3.3.1 2D-MOT

The cooling and repumping light is split in four beams. The light passes through a series of cylindrical telescopes and obtains an elongated profile where atoms can be trapped in a cigar-shaped cloud. The cooling laser of the two-dimensional MOT operates in higher power and higher detuning allowing atoms to cool by scattering more photons.

The atom cloud is aligned with the aperture leading to the main chamber. Since atoms are free to move in the longitudinal direction, they can diffuse through the hole into the main chamber due to the pressure difference between the stages. The flow is further enhanced with the push beam.

Atoms inside the 2D-MOT are cooled from room temperature to the mK regime. The purpose of the two dimensional MOT is to support the loading of the three dimensional MOT where the cooling process further reduces the atom temperature.

3.3.2 3D-MOT

Atoms travelling through the aperture will end up in the main chamber. The MOT utilizes 6 counter-propagating beams to capture

atoms in the center of the chamber. Each beam operates at an optical power of approximately 15.3 mW. All the beams are focused at the center of the chamber and they are aligned with respect to the differential pump aperture.

In contrast to the 2D-MOT, the lower detuning of the 3D-MOT lasers provides a deeper trapping potential.

3.4 Transporting Atoms

At the end of the cooling process, atoms trapped in the 3D-MOT have a temperature in the order of 1 mK [4]. A total of approximately 4×10^9 atoms can be trapped into the spherical atom cloud. Cold atoms inside the spherical cloud can be transported above the sample by means of two all-optical traps. The first trap, the ODT is used for transporting atoms in the horizontal plane, from the MOT to the sample side. Atoms can be transferred in proximity of the sample surface by overlapping it with the optical conveyor. Atoms trapped in the optical conveyor can be transported to the sample by changing the modulation frequency of each beam. Different parts of the sample can be reached using the steering mechanism of the lattice beams.

3.4.1 Optical Dipole Trap (ODT)

The ODT is the first of the all-optical traps that the setup consists of. Atoms inside the ODT are mechanically transported. Transport involves accelerating and decelerating the atoms. Thus, we need to ensure that the interaction between the atoms and the optical field is minimum. Low interaction can be realized by minimizing the scattering rate using high detuning. As a result, the laser needs to be operated in a far-detuned wavelength. The trade-off for the low scattering rate is the low trapping potential using moderate powers. Accelerating the atoms, results in increasing their temperature. The trapping potential needs to be deep such that a significant number of atoms stays trapped after reaching the sample. At high detuning levels, a deep trapping potential can only be achieved with high optical powers. The setup is equipped with a high power Ytterbium-doped fiber laser operating at 1070 nm with an optical power of 20 W (IPG Photonics).

Optical Setup

The setup is consists of two layers of optics. The bottom layer is used for selecting the first order and guide it to the middle layer. The beam couples out of the fiber and goes into a water-cooled AOM. The zeroth order is directed to a water-cooled beam dump also at the bottom level. The first order is picked up and transferred to the middle layer. The beam obtains the final shape by passing through a series of telescopes.

The first telescope consists of two weak meniscus lenses for correcting the beam divergence. At the middle layer, the beam height is 55 $\pm$ 1 mm. The beam first passes through a $\lambda/2$ plate. Then it enters a cylindrical telescope which creates an elongated profile in the vertical direction to enhance the overlap with the standing wave trap. Following, the beam enters the spherical telescope where the final dimensions are set. After the telescope, the beam passes through a 400 mm focusing lens mounted on a rail.

The position of the lens can be adjusted by several centimetres to bring the atom cloud to different positions of the sample. Lastly, a pair of mirrors is used for "walking" the beam. The mirrors allow to adjust the height and incidence angle of the beam. The last mirror is mounted on a rotation stage. We use off-axis displacement to shift the beam rotation point so that the arc of the circle drawn by the focal point passes simultaneously through the center of the MOT and over the sample surface. The mirrors are configured such that the height of the dipole trap is minimum to facilitate atom transport using the conveyor. The maximum rotation angle with the ODT is approximately 8.6 degrees. Higher displacement angles are not encouraged since the beam might hit the entrance side walls of the chamber causing a distorted trapping potential.

3.4.2 Optical Conveyor

Atoms loaded into the ODT are transferred with precision over the sample and then into the standing wave trap. The trap consists of two identical counter-propagating beams. The overlap of both beams creates interference and atoms are trapped at the intensity maxima. After the loading, atoms can be transported towards the sample surface by detuning each of the beam with respect to each other. The optical conveyor is realized at two different locations.

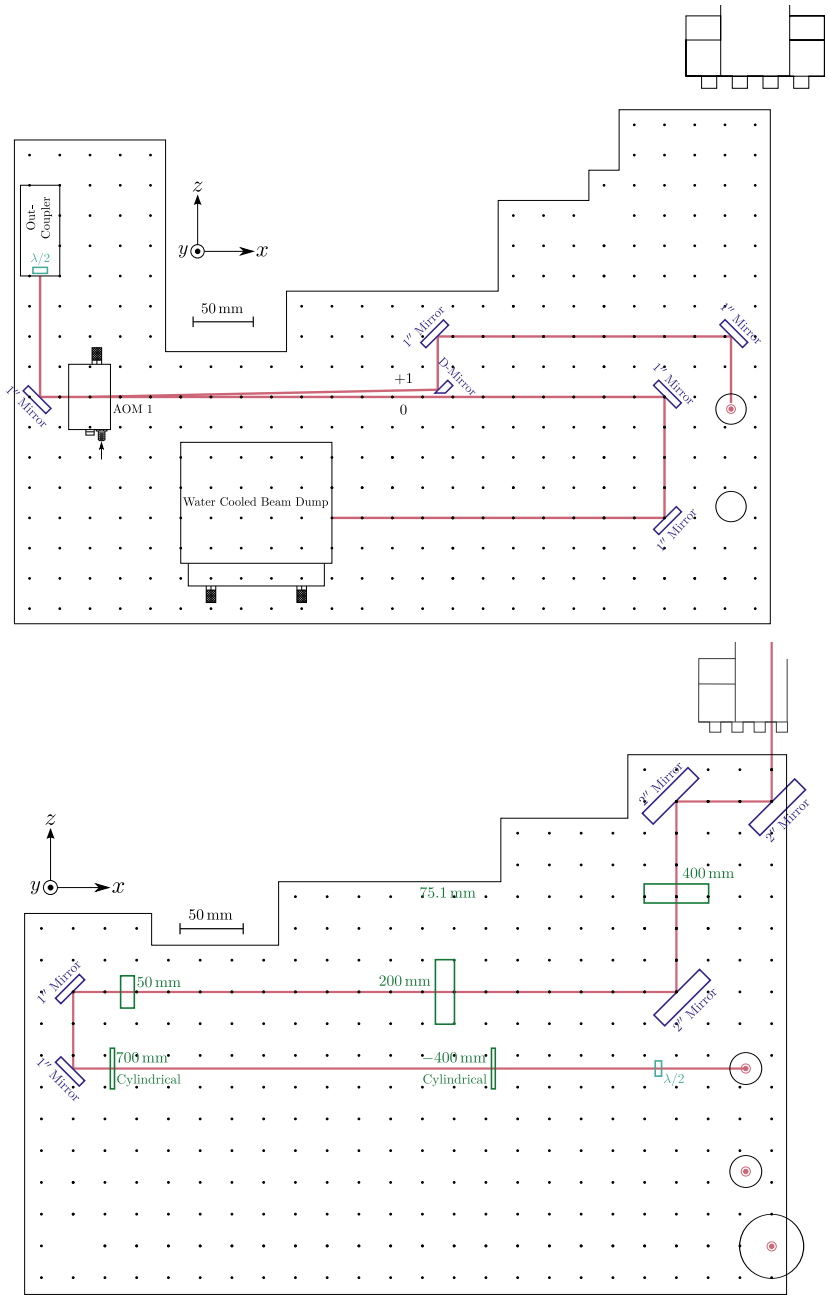

Figure 3.2: Top: Schematic of the bottom layer. Bottom: Schematic of the middle layer. The meniscus lens telescope is placed on the y-axis.

ODT characteristics

Beam Power	15.3 W
Beam height	55 ± 1 mm
Center wavelength	1070.6 nm
Center frequency	1759 THz
Detuning	−104.2 THz
$w_{0,x}$	40 µm
$w_{0,y}$	23.5 µm
Trap Depth	−1.49 mK
Scattering Rate	4.2 Hz
ω_x	3.01 kHz
ω_y	5.08 kHz
ω_z	39.3 Hz

Table 3.2: Optical Dipole Trap specifications. The laser power is measured after the first cylindrical lens. The waist and trap frequencies are adopted from [4].

The light of each arm is created at a dedicated part of the setup. The light is then transported to the main table where the beam diameter is set and steering is realized.

Optical setup-Lattice Table

The beams are produced by splitting a single laser beam as shown in Figure 3.3. A laser consisting of a laser diode and a tapered optical amplifier produces a high powered beam with wavelength λ = 780.52 nm. The beam first passes through an isolator to ensure that no light is reflected back to the optical amplifier. Following, a heated cell containing ^{87}Rb vapour absorbs any resonant wavelengths produced by the amplified spontaneous emission from the optical amplifier. The beam is then split in two beams of equal power with a Polarizing Beam Splitter (PBS). The half-wavelength plate before the PBS shifts the polarization of the incident beam in order to obtain two beams with equal powers (beam balance).

The beams enter two identical arms where they are independently manipulated. Each arm contains a PBS, an AOM, a lens, a mirror and a $\lambda/4$ waveplate. The incident beams hit the waveplate and obtain circular polarization. The diffracted beams of the AOM hit the lens which is focused on the AOM and the angle is converted to displacement. Only the first order is allowed to hit the mirror and reflect back to the AOM.

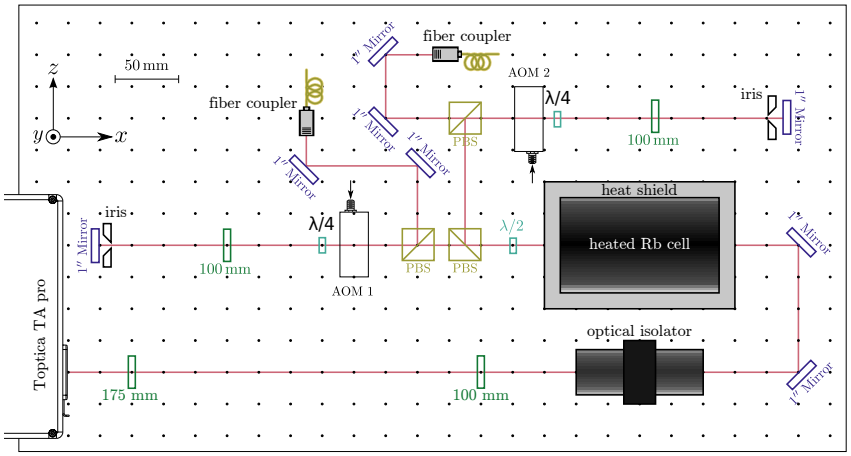

Figure 3.3: Schematic of the lattice beam optical setup.[4]

The detuning is doubled after reflecting the beam again inside the AOM (doublepassing). Higher diffraction orders are cut using diaphragms while only the +1st orders are allowed to reach the mirror. After the doublepassing, the beams hit the $\lambda/4$ waveplate where the circular polarization is converted again to linear. This time having perpendicular polarization. The beams are then reflected at the PBS, go through a pair of walking mirrors and a $\lambda/2$ plate for matching the polarization to that of the polarization-maintaining fiber. Finally, both beams are coupled into fibers and the light is tranfered to the main table. For simplicity only the first-order diffracted beams are shown in Figure 3.3.

Steering the lattice-Main Table

The second part of the conveyor is used for steering each beam in the horizontal (xz) plane. The "scanner" consists of a $4f$ cascade telescope system with two mirror galvanometers. The mirror galvanometers are controlled through an open-loop servo system where

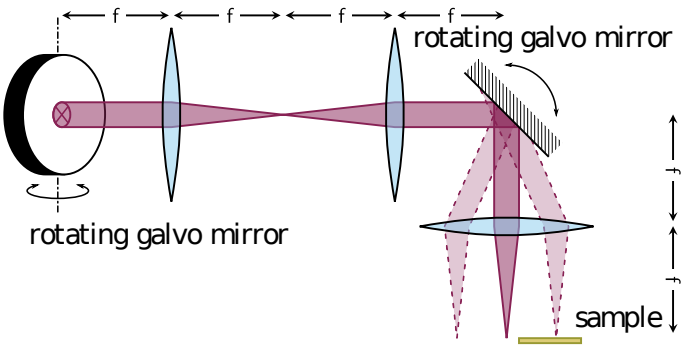

Figure 3.4: The principle of $4f$ telescope system. Adopted from [4]

the input voltage is proportional to the angle of the mirror.

A rotating mirror can change the angle of a beam incident on a lens as can be seen in Figure 3.4. When the rotating mirror is placed at the focal distance of the telescope, the angle of incidence results in translation parallel to the optical axis. The rotation of the mirrors can position the beam in the horizontal plane without introducing any angular displacement. For higher angles, optimization of the beam collinearity is needed to ensure that atoms can transport towards the sample.

Top Arm

The top beam comes out of the outcoupler and a $\lambda/2$ waveplate. It passes through a pair of steering mirrors and enters a telescope where the beam waist is reduced to 500 µm. Then, it passes through a 60 dB isolator and following it enters the 4f-telescope with the galvo system. A Polarizing Beam Splitter is used for splitting the light towards the imaging. The beam exits the "scanner" and folds between three mirrors used to fine-tune the collinearity between the top and bottom beams.

Bottom Arm

The bottom beam is realized at the lower level of the setup. The optical setup of the arm is identical to the top, except of the three last mirrors. Here, one final mirror reflects the beam into the chamber. Since the bottom beam is less accessible, the top beam is always "walked" and aligned to the bottom using the final two final mirrors.

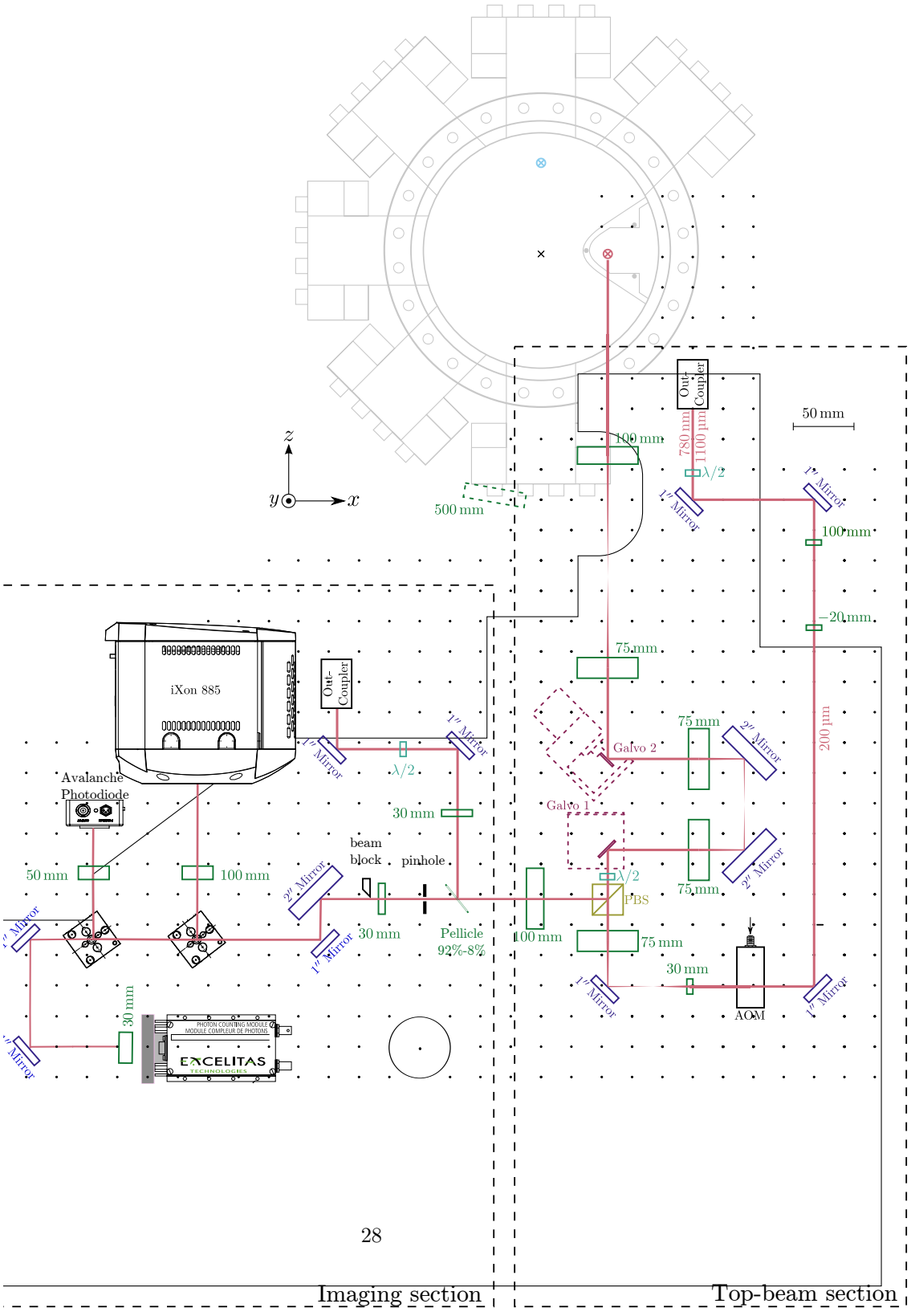

Figure 3.5: Schematic of the top layer of the setup containing the path of the top arm of the lattice and the imaging section.

Lattice beams characteristics

Center wavelength, λ_c	780.6368 [nm]
Center frequency	$2\pi\cdot$ 384.0358 $\pm$ 0.0003 [THz]
Detuning	-0.1111 THz
Linewidth	$2\pi\cdot$300 MHz
Trap Depth	-7.93 mK
Bottom Beam Power	45.8 mW
Top Beam Waist	30.61 $\pm$ 0.13 μm
Bottom Beam Waist	31.25 $\pm$ 0.11 μm

Table 3.3: Lattice Specifications. The wavelenth was measured with a wavemeter. The top beam powers were measured in pulsed mode using a photodiode. The beam waists were determined by beam profiling using a gaussian fit.

The properties of the lattice beams are summarized in Table 3.3.

Loading the conveyor

The optical lattice is loaded by turning on the lattice beams while the dipole trap is still on. Atoms are "transferred" to the lattice since a deeper trapping attracts them into it. The loading time is fixed to 3 ms. There are two different types of loading the lattice, the cascade (single) and the simultaneous (double) loading.

Cascade (single) loading

When atoms in the dipole trap are brought into position, the top beam is turned on $t_{load} = 50$ ms before the dipole trap switches off. During the loading process, atoms captured in the top beam are allowed to diffuse increasing the trapped population. Diffusion results in a slightly longer atom cloud inside the lattice. The bottom beam ramps up to full power 400 µs before the dipole trap switches off. The lattice is formed during power ramp-up of the bottom beam. Atoms will diffuse and reposition at the intensity maxima.

Simultaneous (Double) loading

The two beams are ramped up simultaneously $t_{\mathrm{load}} = 50\,\mathrm{ms}$ before the dipole trap switches off. Atoms are directly loaded into the lattice. The total number of atoms is usually slightly lower but the atom cloud is more dense.

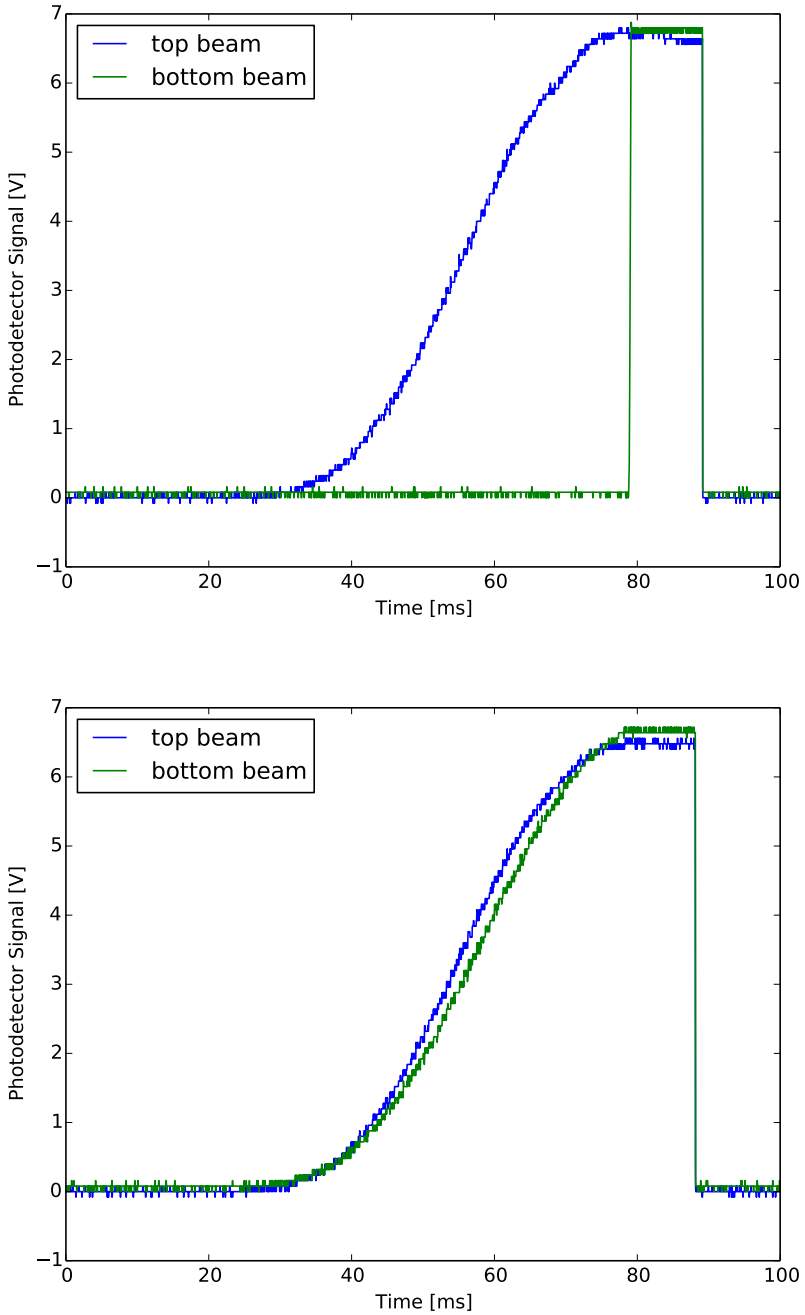

Figure 3.6: Top:Cascade loading, bottom: Double loading. Graphs show the ramp-up of the top and bottom arm of the lattice. The signal was picked up by two photodiodes connected to an oscilloscope. Both diodes are placed before the $4f$ system of each arm.

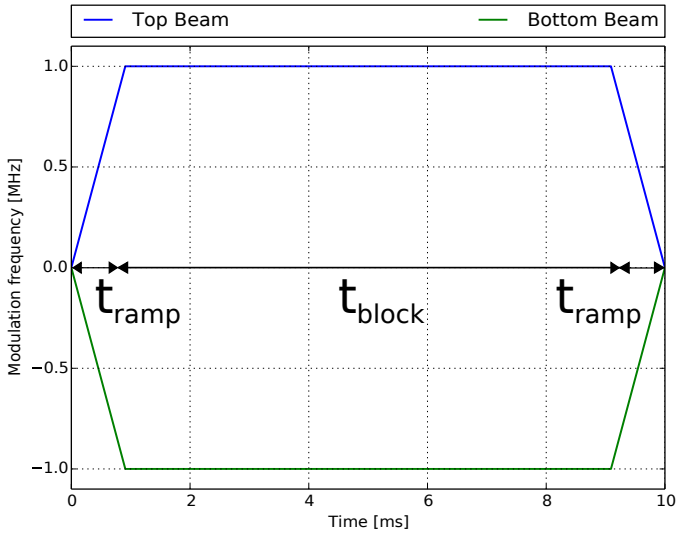

Figure 3.7: Principle of the conveyor motion.

Conveyor Motion Principle

The lattice can be displaced by applying a small Δf between the two beams. Beating is achieved with a Direct Digital Synthesizer (DDS). The DDS produces a low frequency RF signal which is fed to the AOM driver. There the signal mixes with the 80 MHz driving signal and the output frequency is the sum of the two inputs. The beating signal can be set to 1-2% of driving frequency without compromising the AOM diffraction efficiency (approximately 80% for the first order).

Doublepassing the beams to each AOM results in increasing the detuning by twofold. Then, the total frequency difference experienced by the atoms will be $\Delta f_a = 4\Delta f_{DDS}$, resulting in velocity:

$$\upsilon_a = \lambda_C \Delta f_a. \tag{3.1}$$

The lattice is displaced with a trapezoidal motion. The detuning of the top beam is increased gradually to the maximum value with a standard ramp time of 1000 ms. The maximum frequency is then maintained for a specified time called "block time" and finally, it is gradually ramped down. The bottom beam follows the same pattern but with a detuning of opposite sign.

3.5 Atom Imaging

3.5.1 Operating Principle

During absorption imaging atoms are exposed to resonant light. Light gets scattered by the atom cloud and produces a shadow. The shadow is projected to the imaging camera. A good estimate of the atom number can be obtained by calculating the transmitted power when the probe intensity is below I_{sat}. The transmittance, T, of the cloud would then be equal to:

$$T = \frac{I}{I_0} = e^{-\rho_o}, \tag{3.2}$$

where I is the transmitted intensity on the camera, I_0 the probe intensity and ρ_o the optical density of each pixel of the camera. The method is based on collecting three consecutive images. The first two are taken with probe light; one with atoms followed by one reference where no atoms are captured. The third picture with no imaging (probe) light is used for subtracting the optical density caused by the background (stray light, ambient light, detector dark current etc) [14]. Finally, the optical density is calculated as:

$$\rho_o = -ln(\frac{I_{atoms} - I_{bg}}{I_{ref} - I_{bg}}) \tag{3.3}$$

Atoms exposed to resonant light get to the excited state and are lost from the trap. Snapshots of different stages of the experiment can be obtained by probing the atoms after displacements at different distances.

3.5.2 Atom number determination

The number of atoms inside a region of a picture can be estimated by comparing the optical densities between regions with atoms and regions with no atoms. The regions of interest are selected by applying a "mask" (a boolean array with identical shape to that forming the picture). The optical density of the pixel is taken into account only if the corresponding value of the mask is "True".

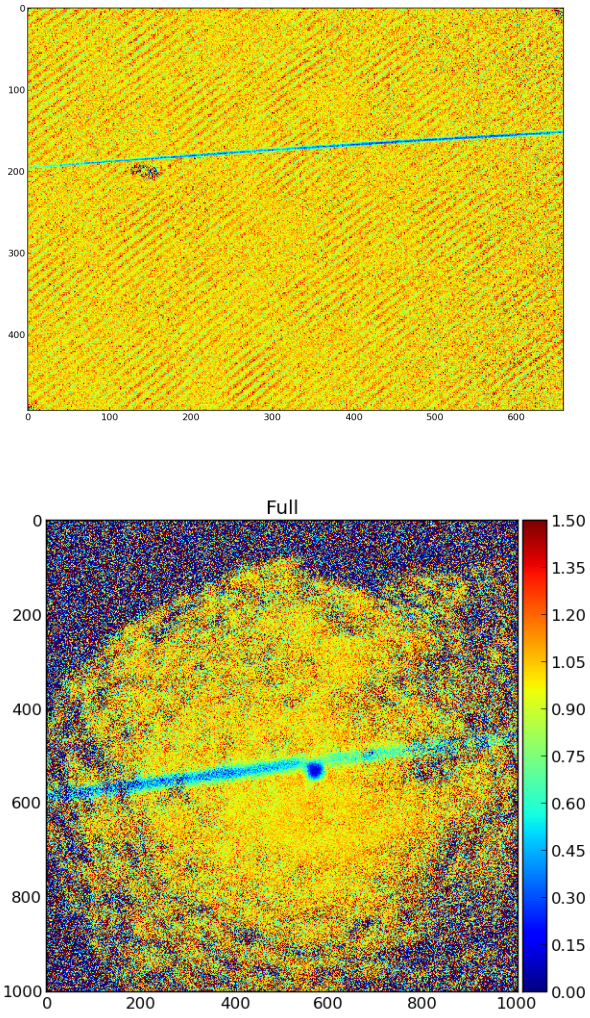

Figure 3.8: Power transmission images. Top: atoms loaded in the dipole trap. Bottom: atoms being transferred to the lattice.

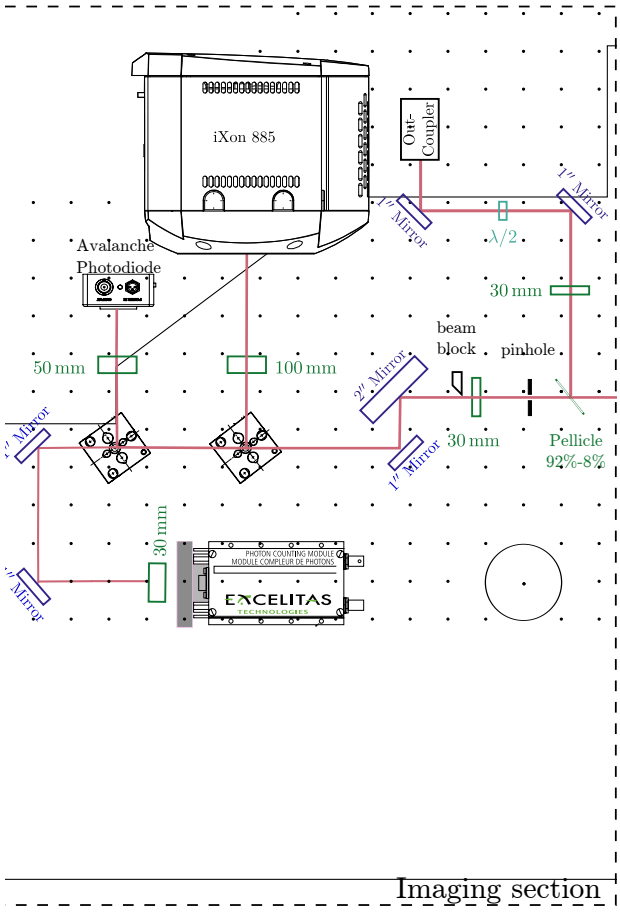

Figure 3.9: Imaging setup. Magnetic mounts in front of the camera and APD allow to select between mirror or Pellicle Beam Splitter. The camera can operate in combination with the photodetectors. When no mirrors/pelicles are mounted on the magnetic mounts, all the incident light will hit the single-photon detector.

3.6 Imaging-Optical Setups

Pictures of trapped atoms can be taken at two different locations of the setup. The first imaging point is located at the center of the chamber where the ODT loads atoms from the 3D-MOT while the second is located above the sample.

3.6.1 Imaging at the center

Imaging at the center of the chamber is necessary for determining the number of atoms loaded into the ODT. The imaging system of the dipole trap consists of a camera (Procilica EC650) and one lens mounted over the top window of the main chamber. The atom cloud is probed for 50 ms with an intensity of 13.6 $\mu W/cm^2$. The image is produced using an algorithm that implements eq. 3.3.

3.6.2 Imaging above the sample

The optical setup is realized at two level of optics. The imaging beam is coupled out at the middle layer. It passes through a pair of steering mirrors, a $\lambda/2$ waveplate and a shutter to completely block the resonant light during loading and transport. The light is reflected to the bottom level where it enters the path of the bottom beam using an PBS. The imaging light is steered together with the bottom beam. The Rayleigh range of the beam is long to ensure that the intensity that the atoms experience is constant at different heights.

The imaging light exits the chamber and enters the top beam path. It is deflected to the imaging system through the imaging beam PBS. There, a spherical lens creates an image plane. The imaging and the bottom beam follow similar paths so a small portion of the bottom beam light hits the camera. A small angle of the imaging with respect to the bottom beam allows to block the bottom beam before the camera. Furthermore, it provides a better picture of the atom cloud during its displacement. The position of the beam block coincides with the image plane of the bottom beam and the Fourier plane of the imaging beam. A focusing lens mounted on a rail is used for changing the position of the image plane. The imaging beam folds between two mirrors for fine-tuning the position of the image on the camera. The imaging setup consists of three

devices. The Andor iXon 885 camera, an Avalanche Photodetector (APD) and a Single-Photon Detector. More information on the the APD and single photon detector will be discussed in section 3.6.4. Figure 3.9 shows the current configuration.

3.6.3 Transmission setup

A dedicated beam path was built for coupling light into the waveguide membranes. Resonant light is transferred with a fiber to the top level of the main table. The collimated beam is coupled out of the fiber and passes through a $\lambda/2$ waveplate, through two mirrors and a 150 mm focusing lens.

The beam is reflected to the imaging path with a 92%-8% Pellicle Beam Splitter and enters the path of the top arm via the beam splitter cube seen in Figure 3.5. The probe beam is overlapped to the top arm of the lattice beams. The steering mirrors are used to optimize the angle and position of the beam over the incoupling grating launchpad.

3.6.4 Transmission Imaging

Our experiments include monitoring the light intensity coupled out of a waveguide. The output light of the waveguide is collected at the imaging setup. Interactions between light and cold Rubidium atoms can be detected at a time scale much faster than the speed of our camera. For this reason, the imaging path contains two photodetectors that share the same path with the camera. The first detector is an Avalanche Photodiode (APD) (Thorlabs APD130A). The APD uses an embedded high gain transimpedance amplifier which allows it to detect low powered signals. The APD is connected to a lock-in amplifier (Stanford Instruments). The internal pulse generator of the lock-in modulates the incoupled beam. The de-modulated signal is sent to a Data Aquisition Unit (DAQ). [3]. The DAQ can detect analog signals with a sampling rate of 250 kHz. This resolution should, in principle, be enough for simple coarse experiments.

The power of the outcoupling spot was measured to be approximately 20 nW after the camera. The Signal-to-Noise ratio of the APD is very low, slightly above the noise floor. A second, more

[3] National Instruments NI-USB-6211

sensitive, detector was added to the setup increasing its capability. The single photon detector can detect single photons with quantum efficiency of $\approx 80\%$. The column density of the detector saturates after absorbing a single photon. The output signal is a logical Time-to-Live pulse which indicates a photon "event". The signal is picked up by the digital inputs of the DAQ with a sampling rate of 50 MHz, enabling us to detect signals indicating interactions at a single-atom-level.

Figure 3.9 shows the setup configuration. The three devices are aligned the same beam path. Two bases with magnetic mounts allow the user to choose between different devices using a mirror or a pellicle beam splitter. If the photodetectors are not needed, a mirror will reflect all the light to the camera. Coarse alignment of the outcoupling spot can be performed by combining the Camera and the APD. If nothing is mounted on the magnetic mounts, all the light will be collected by the single photon detector.

A pinhole at the image plane acts as a spatial filter blocks the unwanted background from the high powered lasers (bottom beam, Optical Dipole Trap) and allows only the outcoupling light to reach the detectors

3.6.5 Nanophotonic Samples

Two different samples were employed for our experiments. First, we used an anti-reflecting coated window to optimize and calibrate the atom imaging and the optical conveyor.

Anti-Reflecting Coated Window

The coating produces a reflectivity as low as $R \approx 0.14\%$ at 780 nm. [15]. This sample was used to check whether a static lattice was formed due to the reflection of the top beam on the sample.

Nanophotonic Waveguide

The sample is located inside the vacuum chamber and the only available port for coupling light is the top window of the chamber. Light can couple into the waveguide membrane when the phase between the optical mode in the slab and the free-space is matched. Approximately at normal incidence this can be achieved using grating

Figure 3.10: The sample containing nanophotonic waveguides placed inside the vaccum chamber.

launchpads.

Grating lauchpads

A series of grating lauchpads have been fabricated with Focused Ion Beam (FIB) milling at the Nanocenter of FOM, AMOLF in Amsterdam. Each 80 μm launchpad features 10 lines. Transmission through each grating coupler was tested at different incident angles θ_x, θ_y and wavelengths. The optimal fabrication parameter settings were experimentally determined to be a groove depth of approximately 175 nm, pitch of 641 nm with duty cycle of $\frac{1}{2}$ with groove depth of 3/4. Figure 3.11 shows a test structure with grating launchpads fabricated at distances 20, 30, 50 and 100 µm where the transmission was tested. Incoupling was achieved at incidence angles smaller than 3 degrees and the total coupling efficiency was approximately 3%.

Coupling of the TE or TM mode can be selected by selecting the polarization of the incident beam with a $\lambda/2$ waveplate located after the outcoupler. Figure 3.12 illustrates how light couples in and out of the dielectric waveguide.

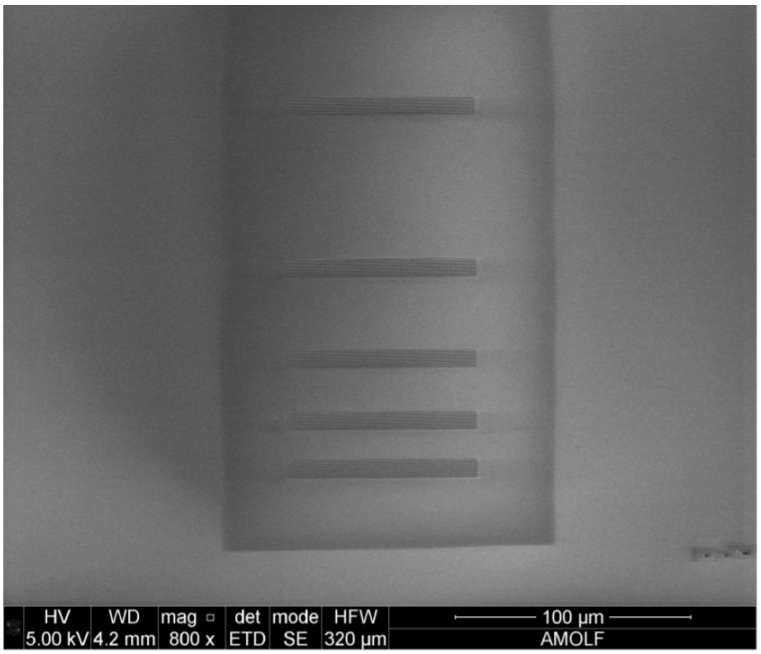

Figure 3.11: Test structure with grating launchpads.

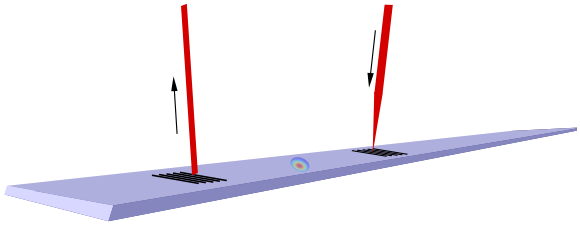

Figure 3.12: Artist's impression of light coupled into the slab waveguide.

Chapter 4

Results

This chapter outlines the experimental procedure used for displacing atoms using the optical conveyor. The initial challenges in the conveyor operation are illustrated along with our strategy for improving the operation of the conveyor. The probe intensity was calibrated using the atoms as a reference. Using the calibrated atom number analysis routines, we determine two different trapezoidal motion profiles, having a constant block time or constant beam hold time.

The optimal properties of the trapezoidal motion (maximum velocity, motion profile and required steps) were determined. Using the optimal settings the conveyor was driven to a final position above the sample. We observed that no additional losses are induced after decelerating at the final position. Finally, the atom cloud was set in motion to move the atoms down and hit the sample surface. We estimated the length of the atom cloud from the atom loss rate and compared it to the waist of the dipole trap. Last, we have succeeded in detecting outcoupled light from a membrane waveguide. We performed an experiment where the transmission signal was recorded without the presence of atoms near the waveguide. This measurement shows the setup performance and will be used as a reference for future experiments involving atoms in the proximity of the evanescent field of the waveguide.

4.1 Challenges

Interactions of light with atoms can be probed by positioning atoms in proximity of a sample with sub-wavelength accuracy. The work

contained in this chapter outlines all the necessary steps towards achieving transport of sufficient numbers of atoms over distances in the order of 10 mm and setting up the experiments for the atom-light interactions. Previous work by Mussmann [4] and Greveling [5] showed that displacing the lattice is possible.

Several changes to the setup improved the performance considerably. Stable and efficient operation of the optical conveyor requires the loss mechanisms to be well controlled; two of them are addressed below.

4.1.1 Parametric Heating

Modulating the standing wave trap with frequencies close to the trap frequency induces resonant heating. An elegant experiment conducted by Mussmann [4] revealed that atoms can absorb energy from the field when the field is modulated with a frequency close to the trap frequency. The absorbed energy will increase their temperature and possibly allow them to escape the trap. The result is that reduced numbers of atoms stay inside the trap after the modulation, as illustrated in Figure 4.1.

Atoms captured in the lattice are modulated for 1 ms and then the atom number is measured. The modulation frequency of both lattice beams is the same, thus the atom cloud is not moving. The experiment is repeated for different modulation frequencies. The experiment targeted in identifying those resonant frequencies and their influence on the atom number and atom cloud size. It was shown that resonances appear in two frequency regions: a narrow dip at several kHz and a wider dip at several MHz.

The first dip is attributed to resonances in the longitudinal direction of the standing wave trap whereas the second to the radial direction. In the latter case the atom cloud expanded, supporting the hypothesis of resonances occurring in the radial direction.

4.1.2 Static Lattices

Another complicating factor in the lattice operation is unwanted static lattices. These lattices arise from reflections on optical elements at different points of the setup. Both lattices interfere with each other and cause the moving trapping potential to be periodically modulated. Simulations suggest that weak static lattices per-

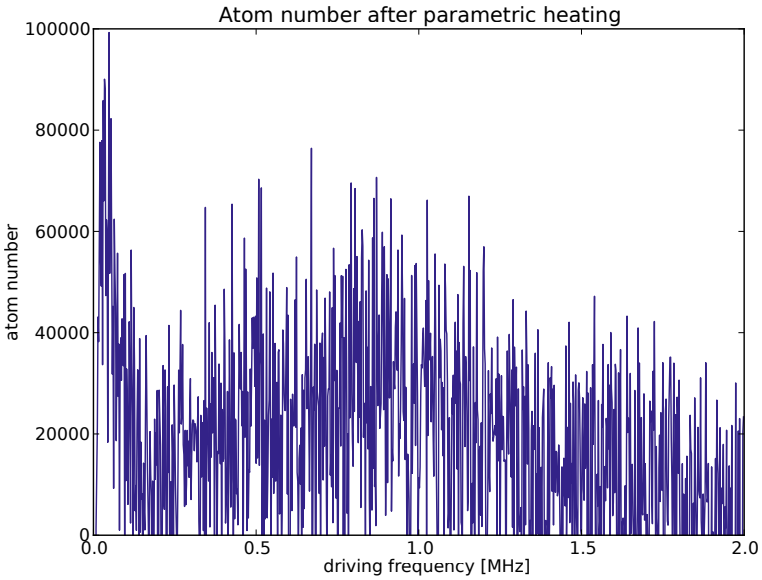

Figure 4.1: Atoms losses plotted as a function of the modulation frequency of the lattice beams. Two regions of losses are witnessed; one narrow resonance in the kHz regime and one wide resonance for frequencies above 1 MHz. (figure adopted from [4].

turb the atoms trapped inside a moving lattice. These perturbations cause atoms to diffuse towards these rigid lattices. Their formation is attributed to reflections on flat surfaces found in the path of the lattice beams [4].

4.2 Atom number calibration

The first step of our study is to calibrate the intensity of the probe beam as this is essential for the accurate and reproducible determination of the intensity of the imaging beam *at the atom cloud position*. Since the atom cloud is in the vacuum chamber, we cannot simply measure the beam power and beam size at this position. We can only measure the beam size and power before the beam enters the chamber and calculate how the beam propagates through the optical elements. This way we get an estimate for the beam intensity at the atoms' location.

However, the atoms themselves provide a more precise and direct method to calibrate the imaging beam intensity, as shown below. The number of atoms can be calculated from the optical density. This calculation depends on the intensity of the probe light. Day-to-day fluctuations in the probe beam power might influence the calculated atom numbers. A calibration experiment was conducted to determine the intensity experienced by the atoms and how much should the probe beam power. A low probe beam power results in lower error in the atom number calculation. On the other hand, low power results in inferior image quality.

From the theory of the 2-level system found in Section 2.1, Figure 2.2 we know that for low intensities, the scattered power depends linearly on the probe power. The power saturates for intensities beyond the I_{sat}, reaching a maximum of approximately 2.5 pW.

Let us suppose a cloud consisting of N atoms trapped in the lattice. There is a relation between the calculated number of atoms (N_{calc}) and the real atom number (N_{real}) that depends on the intensity of the imaging beam. In our experiment we can measure the power of the imaging beam before the beam enters the chamber, but the exact intensity seen by the atoms is unknown. On the other hand, it is known that the atom number will saturate for high intensities.

We define α to be a correction factor to the unknown intensity

experienced by the atoms. The correction is primarily influenced by the difference in the beam size, but α also corrects for the power lost at the optical elements. The calculated atom number does not depend on the probe intensity. Thus, we need to find the value α for which the fraction $\frac{N_{\text{real}}}{N_{\text{calc}}}$ is 1.0.

Our sample consists of pairs of membrane waveguides spaced at a distance of 2 mm. The imaging beam is pointed to the membrane of interest. We placed a power meter at the image plane, hitting the photodetector with light coming only through that pair of waveguides. We compared the intensity collected at membranes to the intensity collected at the imaging beam outcoupler, as shown by:

$$\frac{P_{\text{membranes}}}{P_{\text{probe, outcoupler}}} = \frac{A_{\text{membranes}}}{A_{\text{photodetector}}} \tag{4.1}$$

We determined that the intensities show good agreement. This means that the contribution of the neighbouring membranes is small and that the intensity calculation is accurate. We have measured the intensity coming through the pair of membranes of interest to be $I_{\text{memb}} = 1.2\,\text{mW/cm}^2$.

The real atom number is related to the calculated atom number via the following relation:

$$\frac{N_{\text{real}}}{N_{\text{calc}}} = \frac{1 + \frac{\alpha I_{\text{out}}}{I_{\text{sat}}}}{1 + \frac{I_{\text{memb}}}{I_{\text{sat}}}}. \tag{4.2}$$

The power of the probe beam is manually adjusted using a potentiometer that controls the AOM. The experiment was conducted within the AOM linear region (knob values between 2.5 and 6.5). The measurement was conducted by loading atoms directly into the lattice (double loading), taking measurements for ten consecutive runs, and changing the probe power.

The atom number fluctuations depended primarily on run-to-run fluctuations. The standard deviation across 10 runs was 8%. The normalized values were plotted for the different values of α and the optimum value was graphically determined to be approximately 14 cm^{-2}, since for that value, the normalized atom number oscillated around a constant value 1.0.[1]

[1]These experiments were conducted with a Neutral Density filter (ND10) placed before the fiber incoupling. The optical power was measured after the outcoupler 40.5 µW, with the AOM driver knob positioned at 3.00.

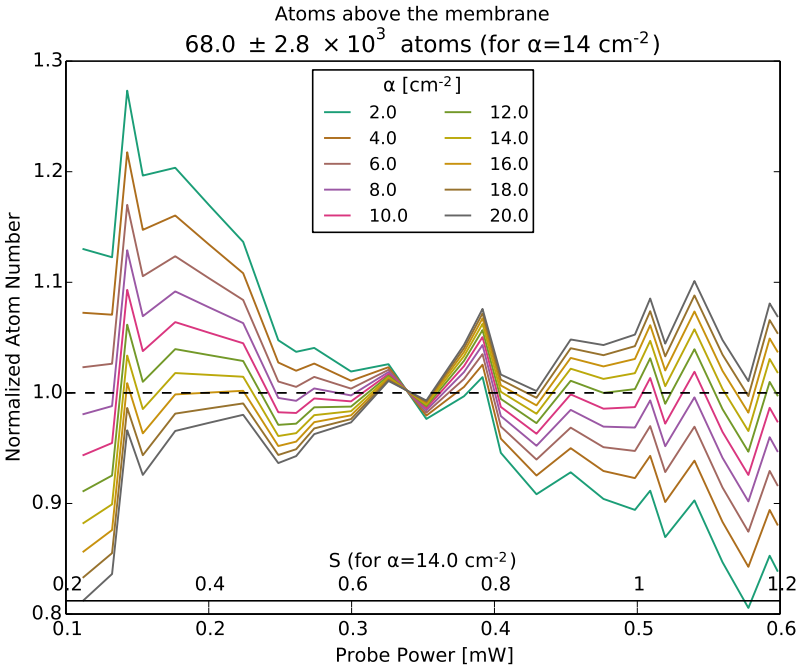

Figure 4.2: Intensity calibration fit.

While the correction factor α has surface area dimensions, it also corrects for the optical power in the chamber since the fraction of power lost at various optical elements between the measuring point and the interior of the chamber is unknown. The calibration was performed with two different samples, while no sample in the chamber gave the same results. This leads to the conclusion that the samples have no influence on the determined values. The used method leads to a consistent calculation for the atom numbers as it takes into account the power needed for atoms to saturate. Our calculation is related to the transition strength described in [8].

Since many experimental parameters were involved in relating the correction factor α to the strength of the transition of different substates during absorption imaging as discussed by Mussmann [4] (laser detuning within a few MHz, precise beam polarization etc), no time was invested in this further.

4.3 Displacing atoms trapped inside the conveyor

The conveyor can transport atoms towards the sample surface. During the transport, atoms are lost due to various loss mechanisms. Here, we define the conveyor motion settings. Our experimental approach starts with defining the three properties for a motion on a straight line: time, maximum speed, and acceleration.

The total time atoms can be held inside the conveyor is limited due to collisions of trapped atoms with atoms/molecules in the surrounding environment and many-body interactions between atoms trapped inside the lattice. A significant population can be maintained for times below $t_{\mathrm{hold}} = 10\,\mathrm{ms}$. The total motion is performed within this time interval.

The maximum achievable velocity and acceleration are imposed by parametric heating effects. Modulating atoms with driving frequency above 1 MHz (f_{Atoms}=4 MHz) results in heating up the atoms. Thus, the maximum modulation frequency needs to stay below 1 MHz.

Our approach uses a motion with trapezoidal profile and discrete ramps. Both AOMs are shifted in frequency. The motion can be initiated by ramping the AOM modulation frequency through different

values, until a maximum frequency corresponding to υ_{max} as:

$$\upsilon_{\max} = \lambda \cdot f_{\text{atoms}}, \tag{4.3}$$

where $\lambda = 780.5$ nm.

During the ramp, the frequency will pass through the low-frequency resonance found in the order of a few kHz. The trap will experience a narrow resonance which limits the trap depth and allow atoms to escape the trap. The discrete nature of the ramp allows us to ramp quickly through it and minimize the losses. Furthermore, excessive acceleration during the ramp-up causes atoms trapped at the edge of the trap to fall back.

4.3.1 Conveyor motion

The time intervals which are relevant for the lattice displacement are primarily the hold time of the lattice beams, the ramp time and block time of the motion. Seeking to simplify the experiments we chose the ramp time to be 1 ms. The lattice motion takes place using two different approaches.

Constant hold time

The first approach occurs with a constant hold time (typically 10 µs) and a varying block time (see fig 4.3). The velocity of atoms is zero when these arrive at their final position. For simplicity the lattice motions shown, are displaced with modulation frequency of 1 MHz.

Constant block time

The second approach consists of a fixed block time and a varying hold time. When atoms are displaced using a constant block time, the motion interrupted. This means that atoms have some velocity. The motion is illustrated in Figure 4.4.

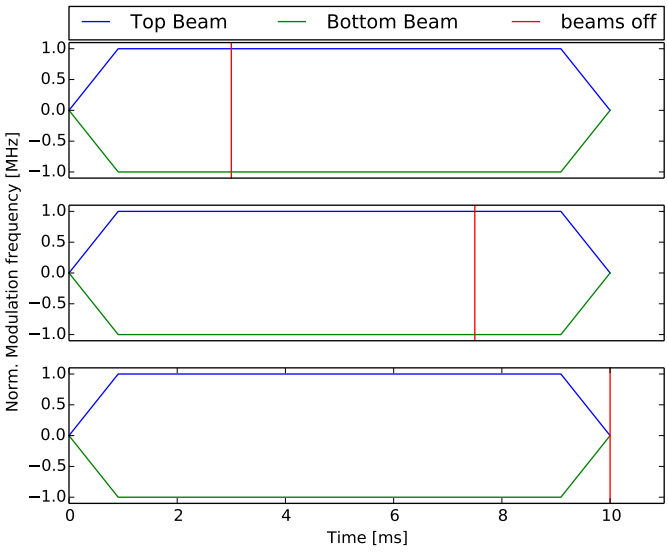

Figure 4.3: Hold time experiment.

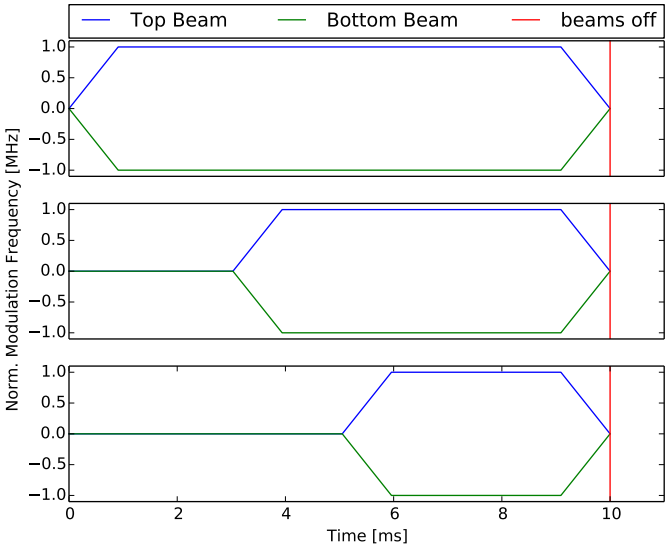

Figure 4.4: Block time experiment.

Loading

During the experiments, we use the lattice loading as a parameter. Single (cascade) loading results in more trapped atoms, whereas double loading loads less atoms. Due to the difference in the trapped population, we can determine whether our results depend (or not) on the loaded populations. Further, we believe (as described in chapter 2) that single loading results in a longer cigar since atoms are allowed to diffuse before the bottom beam ramps up to full power.

4.3.2 Optimizing the conveyor motion parameters

Due to parametric heating effects we need to determine the optimal conditions for displacing the conveyor without significant losses. The parameters are the maximum velocity and the acceleration of the atoms. The conveyor motion initiates with ramping up the modulation frequency of the AOMs. During the ramp, the modulation frequency of the AOMs steps between discrete values. The frequency difference between two adjacent points in the ramp denote the acceleration. Both experiments were performed over the AR coated window sample.

The first experiment aimed in determining how many points are necessary for creating a smooth, optimal ramp. Atoms accelerate towards a "safe" modulation frequency (0.3 MHz) with different number of steps in each run. For the second experiment, we displaced atoms with different frequencies and measured how many atoms remained at the starting position. Each ramp consisted of 20 points to ensure that acceleration during the ramp would not contribute to losses.

The conveyor is used to transport, place and hold atoms precisely above a sample surface. We conducted an experiment to determine whether losses due to diffusion are introduced at the final position of the atom cloud after a trapezoidal motion. The experiment consisted of a motion with constant hold time (10 ms), constant block time of (3.7 ms) and varying time at the bottom. This experiment is identical to the motion performed at a motion with a constant block time.

From these experiments we can reach the following conclusions:

1. All the ramp motions need to feature more than five steps to avoid thermalizing atoms. For future experiments we chose

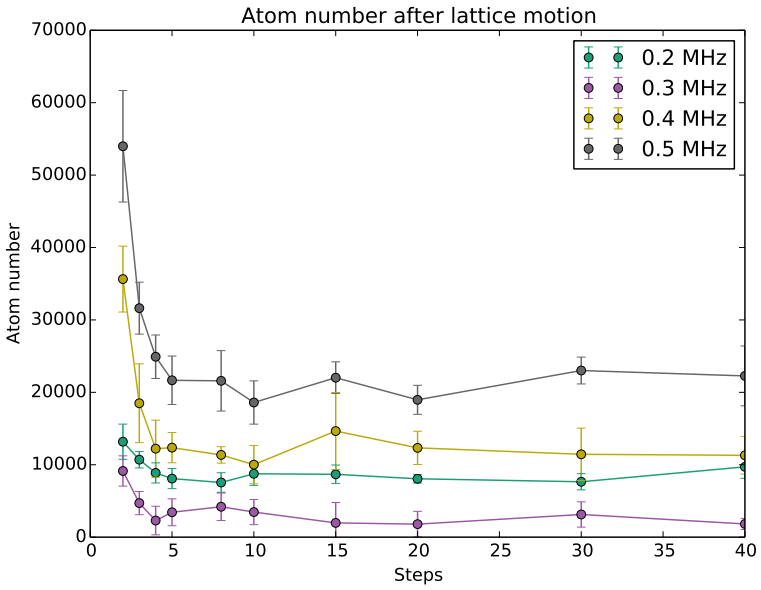

Figure 4.5: Required number of steps for minimum atom losses.

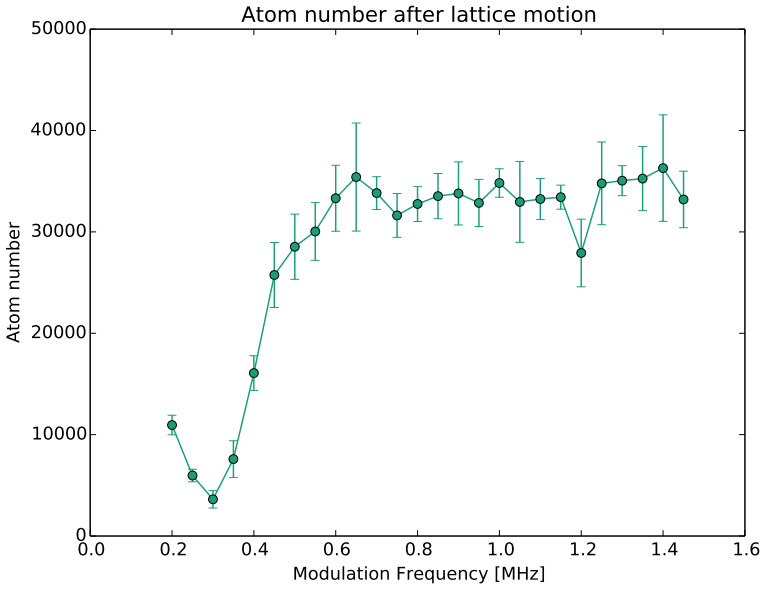

Figure 4.6: Atoms left at initial position after displacements with different modulation frequencies.

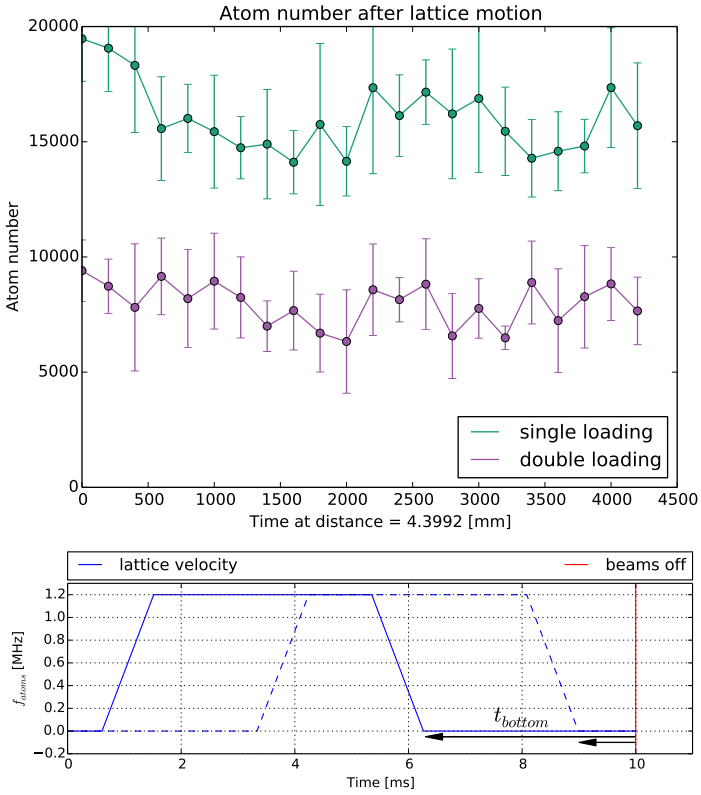

Figure 4.7: Up: Number of atoms inside the lattice held at the final position. Down: Profile of the lattice motion.

to use 20 steps which matches the DDS resolution (50 µs). The effect of losses due parametric heating is mitigated using enough steps.

2. Displacing atoms with modulation frequencies higher than 0.5 MHz (4 MHz for the atoms) are not advised since the trap depth is distorted and leads to significant atom losses.

3. No additional loss mechanisms are induced at the final position after atoms have been displaced above the sample. This finding comes in good agreement with simulations performed by [4], where it was found that a tiny fraction of atoms (approximately 1%) might move from the lattice after a trapezoidal motion.

After having determined the optimal conditions for the conveyor motion, we are able to transfer atoms to the sample surface. We can determine the position of the sample surface with respect to the height where atoms are loaded into the lattice by transferring and "crashing" them on the sample surface. When atoms come into close proximity with the surface, they will escape the trap and graze in the free space or they might get physically adsorbed on the surface of the sample via van der Waals forces.

4.3.3 Elimination of static lattices

Transporting atoms inside the lattice requires optimal mode overlap so that the trap width and the potential were uniform everywhere. In our setup, an optimal alignment produced two powerful unwanted reflections. These were produced from the top beam reflecting on the fiber of the bottom beam and vice versa. We suppressed the reflections by inserting two isolators [2] with attenuation of 60 dB. The result of this addition was a considerable increase in the transported atom numbers. Naturally, there are more optical elements with flat, reflective surfaces which create static lattices, such as the glass surfaces of the chamber or the sample surface itself etc. Those reflections have significantly low powers and their influence was not expected to limit our experiments.

Naturally, there are more optical elements with flat, reflective surfaces which might contribute to static lattice formation such as the glass surfaces of the chamber or the sample surface etc. Those

[2] Toptica Dual-Stage DSR780.

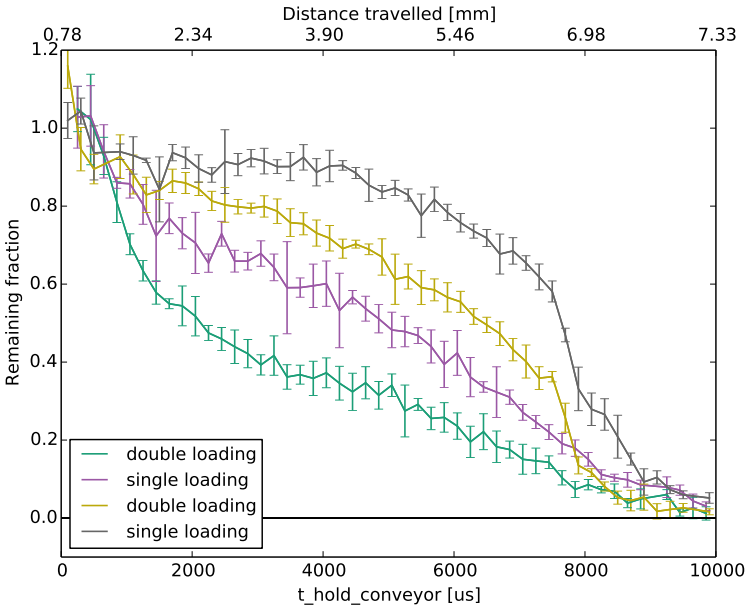

Figure 4.8: Comparison between identical experiments before and after placing the isolators. The purple and cyan lines denote the experiment before the isolators, whereas the grey and yellow curves were obtained after the installation.

reflections have significantly lower powers and their influence was not expected to limit the conveyor operation.

Figure 4.8 shows two identical experiments before and after placing the isolators. The remaining fraction was calculated by normalizing the atoms with respect to the first five points of the measurement. The reader can easily distinguish the significant improvement in the slope. A steeper slope upon inserting the isolators resulted in a "shorter" lattice, as indicated by the legend. This occurs due to suppressing diffusion of atoms towards the powerful static lattices.

During experiments with a varying beam hold time, the conveyor displacement starts as soon as the loading time ends. Atoms originally trapped inside the ODT expand thermally to all directions and also pass through the mask. This causes the detected atom number to increase for short hold times. As those atoms diffuse in free space, their optical density inside the mask fades out quickly without contributing further.

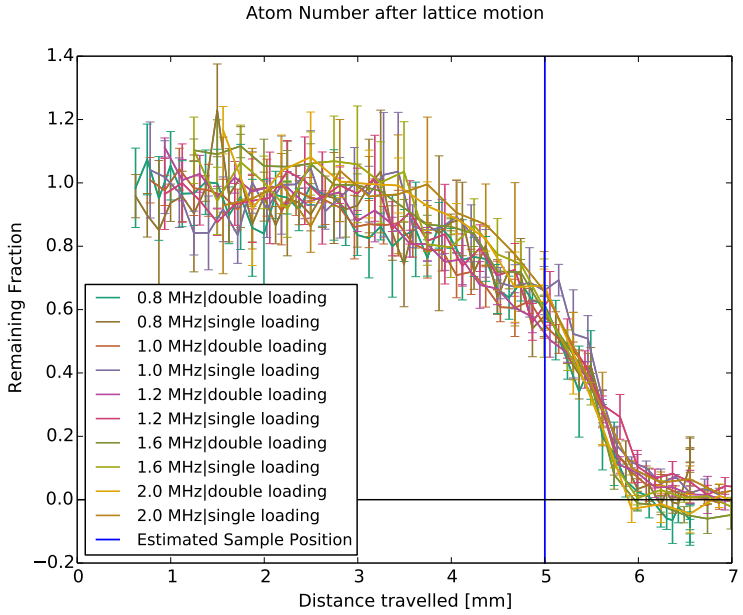

Figure 4.9: Remaining fraction of atoms inside the lattice. The lattice was displaced with a varying block time. Several experiments were conducted with different modulation frequencies.

4.3.4 Influence of the modulation frequency crash curve slope

We performed a set of experiments where the lattice was displaced with a varying block time. Each experiment was conducted with a different modulation frequency (lattice velocity). As long as the displacement velocity stays away of frequency regions where parametric heating is known to thermalize atoms, the velocity has no significant influence on the steepness of the slope as can be seen by the lines converging tightly at an approximate distance of 5.5 mm in Figure 4.9.

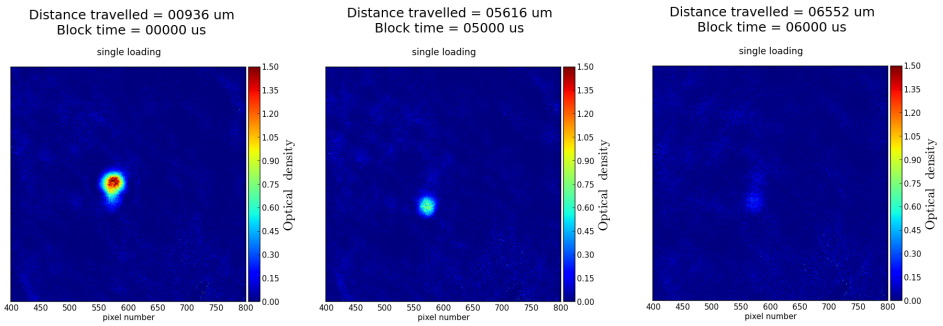

Figure 4.10: Illustration of the atom cloud moving towards the sample surface.

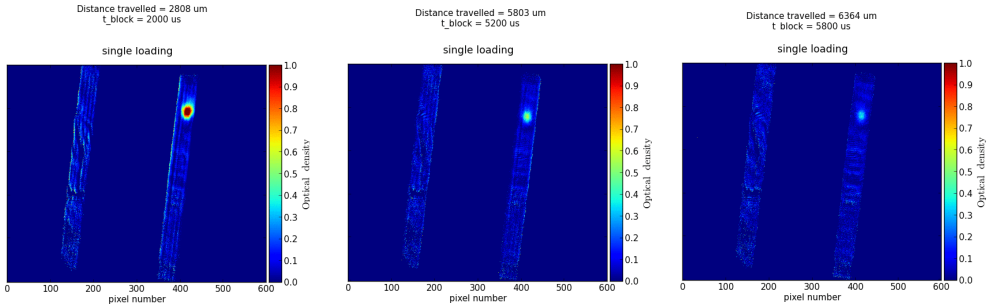

Figure 4.11: Atom cloud moving above a membrane.

As soon as we have optimized the conveyor using the reference sample, we proceeded to performing similar experiments over a waveguide membrane. Atoms were transferred to the sample surface and there were no significant differences between crash curves taken on the AR coated sample. Figure 4.11 shows a similar experiment where we displaced the atom cloud over a membrane.

4.3.5 Atom rates

When the atom cloud descended towards the sample surface, atoms were lost due to parametric heating, diffusion, many body losses etc. The losses contribute to the non-linearity of the curve as can be seen in Figure 4.12. The loss rate was significantly enhanced when the atom cloud hit the sample surface. We quantified the loss rate (in atoms per unit length) by fitting a linear curve at the point where the atoms crash. Since the lattice is displaced with constant

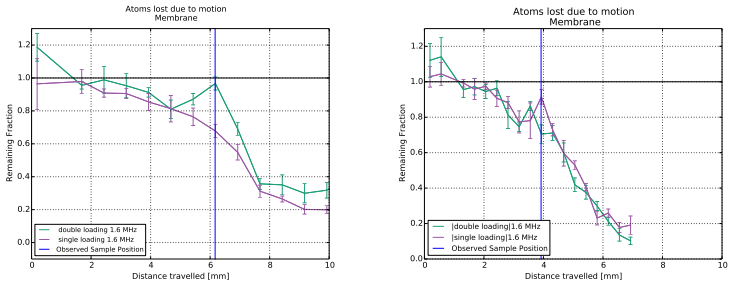

Figure 4.12: Remaining fraction of atoms inside the lattice. The lattice was displaced with a varying hold time.The experiment was conducted over the membrane sample.Left: Before optimizing the ODT height. Right: After optimizing the ODT height.

Max Velocity MHz	Cloud length mm	Atom Rates $10^3 Atoms/ms$
0.8	1.706	38.8
1.0	1.309	62.6
1.2	1.862	58.8
1.6	1.538	82.3
2.0	1.351	102

Table 4.1: Atom Rates with Single Loading.

velocity, $x = \upsilon \cdot t$, atom rates in units of atoms per unit of time were simply obtained as:

$$\frac{N_{\text{Atoms}}}{x} = \frac{N_{\text{Atoms}}}{\upsilon \cdot \Delta t} = \frac{1}{\upsilon} \frac{\text{Atoms}}{\Delta t}. \tag{4.4}$$

In tables 4.1,4.2 the atom rates from several experiments are given in units of atoms per millisecond.

4.3.6 Estimation of the atom cloud length

When fitting the normalized curves, the slope does not depend on the atom number since it has units of inverse length. The inverse slope can provide an estimate of the atom cloud length. We analyzed several of our experiments towards estimating the cloud size. In the following tables we illustrate the observed atom rates and atom cloud dimensions for a series of experiments.

Max Velocity MHz	Cloud length mm	Atom Rate $10^3 Atoms/ms$
0.8	1.670	26.1
1.0	1.700	32.8
1.2	2.000	33.9
1.6	1.399	61.0
2.0	1.058	81.1

Table 4.2: Atom rates with Double Loading.

According to our calculations the cloud number is on average 1.55 ± 0.03 mm long or approximately 4000 ± 80 pancakes. The estimated size is too long, we would expect the dimensions to be significantly less than one millimeter.

A few potential causes can be already outlined. The atom cloud becomes longer during the motion, due to atom diffusion caused by static lattices periodically distorting the trap depth. Even though the two powerful static lattices were eliminated, other rigid static lattices can still perturb the trapping potential. These lattices originate from other flat surfaces in the setup such as the windows of the chamber, the sample etc.

Second, the trap depth of the lattice is much deeper than that of the ODT. The atoms might expand adiabatically resulting in a longer cloud.

In cascade loading, cold atoms are free to diffuse inside the beam until the bottom beam ramps in full power when they become confined inside the lattice. It was proposed that the initial atom diffusion during cascade (single) loading produces a longer atom cloud. For the same reason, double loading is expected to produce a more confined cloud with dimensions closer to those of the dipole trap.

Our limited experimental resolution is one of the factors reducing precision while estimating the cloud length. At this resolution, atom diffusion during cascade loading does not seem to elongate the atom cloud significantly. Based on these experiments we can conclude that there is no pronounced difference between the cloud lengths for cascade or double loading.

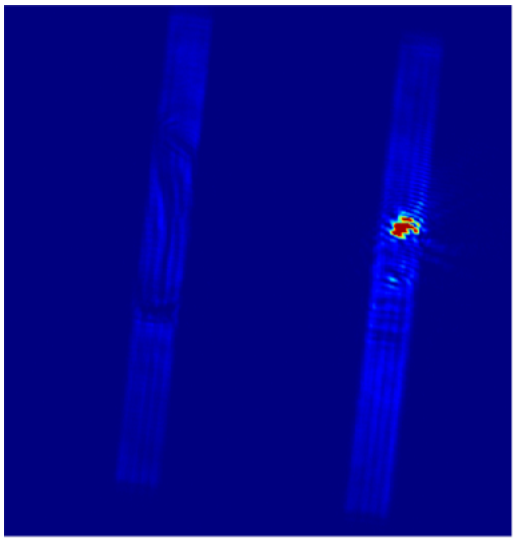

Figure 4.13: Transmission through the membrane waveguide.

4.4 Imaging the transmitted light from a slab membrane waveguide

The last part of the experiment requires light to be coupled into the nanophotonic waveguide. We have identified two membranes where the geometrical parameters of the grating launchpads showed transmission of light. From these two, the membrane showing a higher output power was selected for our experiments. Using the two steering mirrors, we guided the beam towards the grating lauchpads. The incoupling was optimized by changing the angle and position (beam walking) from the walking mirrors while observing the outcoupling from the camera. The power coupling out of the waveguide does not exceed 20 nW. We succeeded in exciting both TE and TM mode through the slab waveguide.

We directed the beam from the outcoupling grating into the avalanche photodiode which was connected to the lock-in amplifier. The DAQ sampled points with 250 kHz for 110 ms. The sampling started just before the conveyor motion initiates. The un-amplified signal is low, slightly above the noise floor of the detector. The low signal-to-noise ratio requires to build statistics over multiple repetitions of each measurement. The signal-to-noise ratio was improved

by summing multiple identical signals.

The motion of the rotation stage of the dipole trap arrived above the sample with an uncertainty of a few hundred microseconds. The time-jitter impacted the lattice loading and the transport. As a result, it also impacted the transmission measurements. The signal from each run was shifted in time. These runs were summed after being "aligned" in the time domain. They were aligned with respect to a reference event present in the signal.

The reference event was created by the return of the rotation stage to its initial position. As this event occured long after the lattice beams switched off, the response was attributed to the mechanical vibrations of the stage influencing the incoupling quality to the slab waveguide. It was, then, a suitable event to use for correcting the jitter as there were no other events interacting with the signal.

Sources of interference

The interference sources were attributed to mechanical and optical effects. During the 3D-coil switch-off time, the current changes abruptly. This created a mechanical force on the table. The impulse response of the table is a damped oscillation. Furthermore, the rotation stage produces vibrations during its motion. We eliminated the influence of the coils by introducing a 20 ms ramp-down time for the current. Moreover, we decoupled the mechanical contact of the rotation stage to the middle layer of optics. The last improvement included two aluminum beams which formed triangulations and increased the stiffness of the layers. These improvements decreased the vibrations seen in the signal, but still allowed them to be detected by our analysis routines.

Our lock-in detection system operates at a lock-in frequency of 530 kHz. That channel was selected since it showed lower background compared to lower lock-in frequencies. During the conveyor ramp-up, the modulation frequency of the top beam AOM passes through 530 kHz. Stray light from various reflections of the setup is picked up by the detector. The average signal contains these two powerful peaks which occurred during the acceleration and deceleration of the lattice.

An example of the total signal is illustrated in Figure 4.14.

A transmission experiment can be realized in three steps:

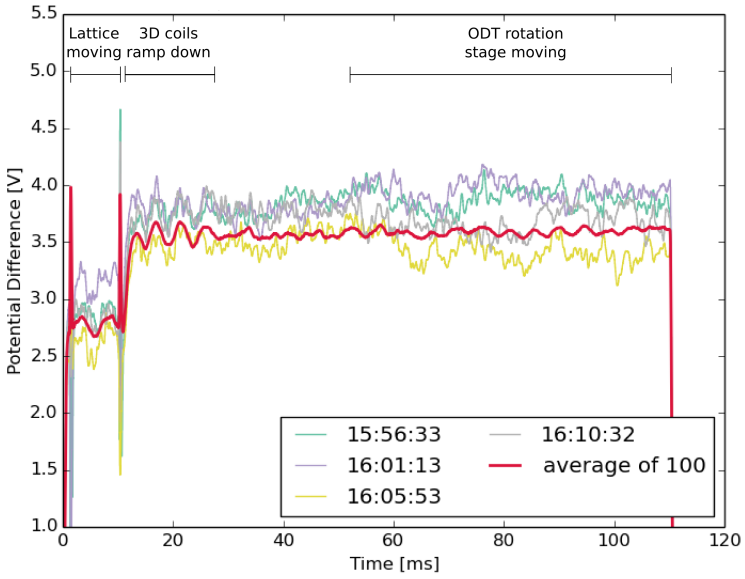

Figure 4.14: Sources of interference in the transmission signal.

1. **Atoms experiment**: Perform an experiment where atoms are transferred and "crashed" over the slab waveguide.

2. **Reference measurement**: Repeat the second experiment while the MOT lasers are electronically disabled. Thus, atoms are not trapped but the events timing, laser light (background) and motions (vibrations) are identical to the interaction measurement.

3. **Interaction measurement**: Repeat the atom experiment while light is allowed to couple in and propagate through the waveguide. During this experiment only the APD or SPD detectors can be used, *not* the camera.

4.4.1 Reference Experiment

We conducted a reference experiment to determine the response of the setup. The measurement was taken by electronically blocking the beams of the two-dimensional and three-dimensional MOTs, thus, not allowing atoms to be trapped. A reference measurement is

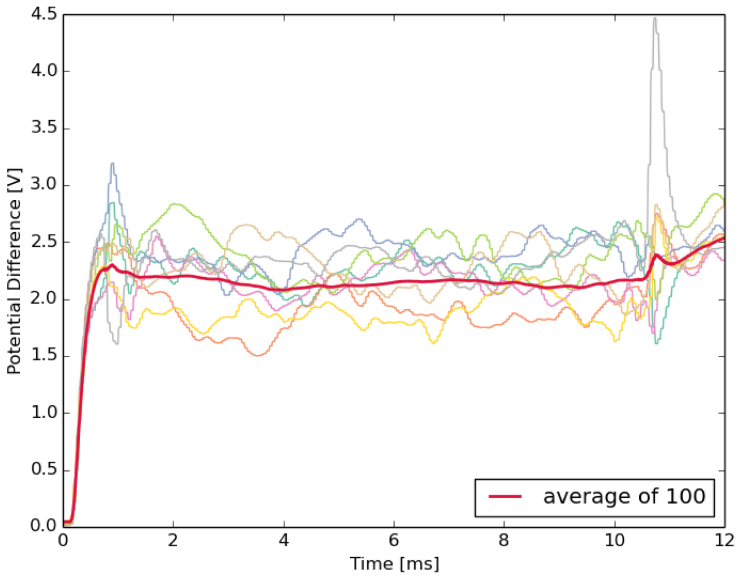

Figure 4.15: Aligned reference signal, taken by averaging 100 runs. The bold red line represents the average of 100 runs. The thinner lines are randomly picked individual runs, plotted for reference.

required for subtracting various sources of interference, background which is not filtered-out and other signals that are not related to the interaction. As can be seen in Figure 4.15, the signal is approximately constant with a value of 2.2 V.

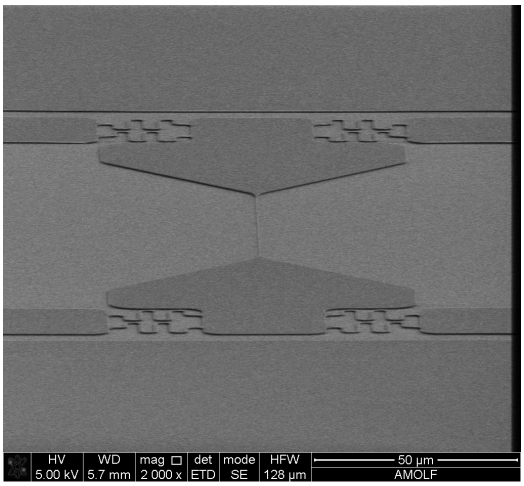

Figure 4.16: Free standing beam waveguide of cross section 200 nm × 200 nm.

4.5 Conclusions and outlook

This experimental work has made the transport of atoms possible. We have accurately determined an intensity correction for the accurate determination of the atom number. The transmission section allows the simultaneous operation of different detectors (eg. camera and APD) as well as the detection of low signals, even at a single photon level. Furthermore, we have implemented the analysis routines to correct for the rotation stage jitter. We can now bring atoms to the proximity of the sample and perform interaction experiments.

A new sample has become available. It features a free standing one-dimensional bridge with cross section dimensions of approximately 200 nm × 200 nm and separation between the gratings of 1 mm. The narrow waveguide allows the mode to be exposed at both x, y directions, allowing for higher overlap between atoms and the optical field. The larger separation can reduce the background light leaking into the transmission detectors due to the outcoupling light and lattice beams being too close. This configuration will enhance the overall signal-to-noise ratio. Furthermore, due to potential low-powered static lattices created by the finite reflectivity of the membrane, the smaller sample surface will provide a significantly smaller reflection.

Acknowledgements

So many experiences in this lab, so many challenges but the all moments spent in there cannot just be forgotten...

First of all, I would like to thank Dries for his guidance, enthousiasm, creative thinking, wild ideas, and joyful moments with games at the corridor. I would like to thank him for giving me all the time I needed for completing this project.

The second person, would then be Arjon. From a daily supervisor to a dear friend. We spent endless hours in the lab with good music, collected tons of measurements, optimized bad "incouplings", and had so many scientific discussions. Arjon, thanks for all your help inside and outside the lab. Thank you for your constructive comments during writing this thesis. I wish you best of luck in your final sets of experiments. Just do it man, just push the button!

Sebas, you were always eager to help when your input was needed. After all, your work was a big part of the lab. I still remember your face when we told you about the optimized operation of the conveyor! :D Thanks for all the funny conversations at your office! And something else; I guess you know about the light-saber already, but if you don't, it was the IR-viewer. Look through and just turn it around and you will see the saber showing up in front of you.

Ole, you were the first one to show me around when I started. Your guidance and input was really valuable in moments where no solutions were obvious. Your work and PhD thesis were the most valuable material available (after this thesis of course) for both the physics and the experimental setup.

Xavi, thanks for your useful advice and expertise. Always there to explain and help; and explain! I still remember your "One-slide-presentations" during the weekly meetings lasting forever.

I would like to thank the other students shared time and space (literally) in the group: Anne, James, Qiao, Koen, Marcel, Jasper (thanks for the bad music and the Russian swear words), Karindra and Gordian. Guys, it was nice to co-exist with you!

Last but not least, I would like to thanks the engineers who supported our work. Paul, Frits and his intern (what was his name again? Ah yes... Dante), and Cees, thanks for your eagerness and creativity when we needed it! Even when the deadline ranged from "Yesterday" to "Now"! Also thanks for stealing your equipment

every now and then and never returning it back.

Appendices

Appendix A

Transitions of the D_2 hyperfine state

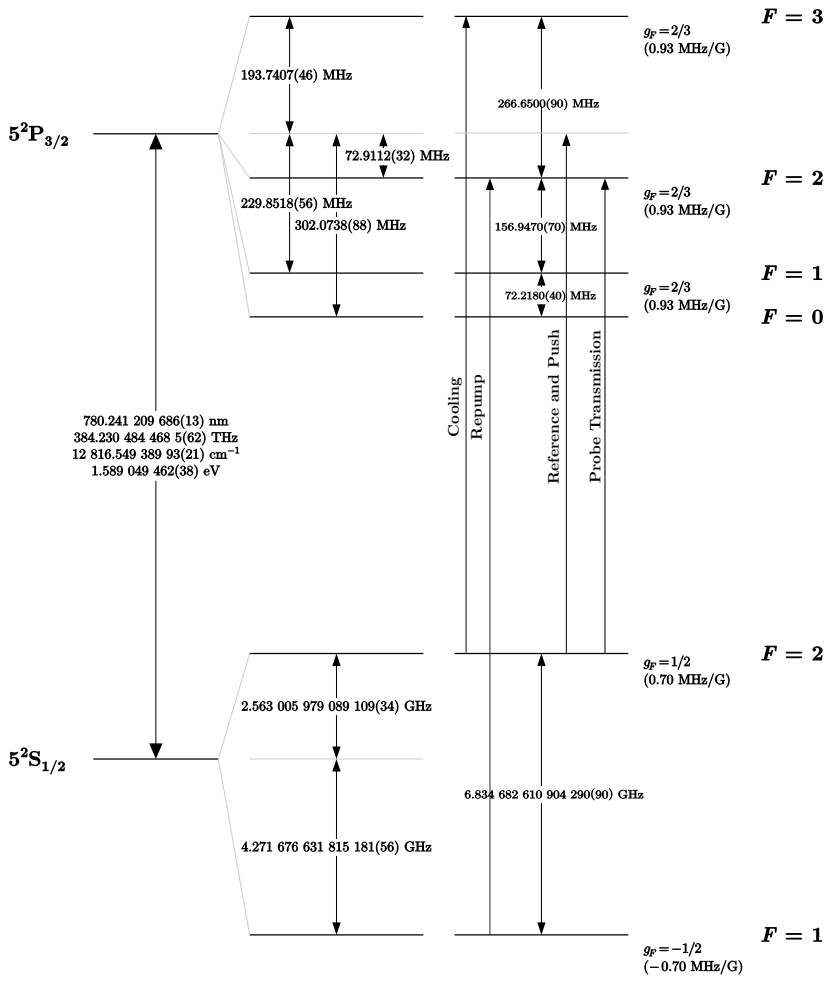

Figure A.1: ^{87}Rb D_2 transitions of the hyperfine state.

Bibliography

[1] M. H. Anderson, J. R. Ensher, M. R. Matthews, C. E. Wieman and E. A. Cornell *Observation of Bose-Einstein Condensation in a Dilute Atomic Vapor*. Science, Vol 269, Issue 5221 (1995).

[2] S. Hooker, C. Webb. *Laser Physics*. Oxford University Press 2010. Pages 548 - 551.

[3] R. Grimm, M. Weidenmuller, Y. B. Ovchinnikov. *Optical Dipole Traps for Neutral Atoms*. Advances in Atomic, Molecular and Optical Physics (2010). Vol. DOI: 10.1016/S1049-250X(08)60186-X

[4] B. O. Mussmann. *A versatile Atom Transport Apparatus for Photonics*. Doctoral Dissertation, (2016), Universiteit Utrecht.

[5] S. Greveling. *An Optical Conveyor for Light - Atom Interaction*. Master Thesis, Utrecht University, Utrecht (2013).

[6] L. Novotny, B. Hecht. *Principles of Nano-Optics*. Cambridge University Press, (2008).

[7] H. J. Metcalf, P. van der Straten. *Laser Cooling and Trapping*. ISBN-0-387-98747-9, Springer, (2013).

[8] H. J. Metcalf and P. van der Straten. Laser Cooling and Trapping. Graduate Texts in Contemporary Physics. Springer New York, 2012.

[9] H. J. Metcalf and P. van der Straten, *Laser Cooling and Trapping of Atoms*. Journal of the Optical Society of America B: Optical Physics vol.20, no.5, pp. 887–908, (2003).

[10] R. Chrétien. *Laser cooling of atoms: Monte-Carlo wavefunction simulations*. Master Thesis, Université de Liège, (2013).

[11] J.P. Dowling, J.Gea-Banacloche. *Evanescent Light-Wave Atom Mirrors, Resonators, Waveguides, and Traps*. Advances in Atomic, Molecular and Optical Physics, Vol 37, (1982).

[12] D.A. Steck. *Rubidium 87 D Line Data*. (Revision 2.1.5, 13 January 2015). http://steck.us/alkalidata/rubidium87numbers.pdf.

[13] D.A. Steck *Quantum and Atom Optics*. Available online at http://steck.us/teaching (revision 0.11.5, 27 November 2016).

[14] *User's Guide, Andor iXon 885. Version 3.6. Andor Technology*. Available online: http://www.oir.caltech.edu/twiki_oir/pub/Palomar/TMAS/TmasElectronics/iXon_M

[15] *Thorlabs Product Description, AR coated window*. Available online: https://www.thorlabs.com/NewGroupPage9.cfm?ObjectGroup_ID=1117